

OPTICAL MORPHOLOGIES OF MILLIJANSKY RADIO GALAXIES OBSERVED BY *HST** AND IN THE *VLA* FIRST SURVEY

J. RUSSELL², R. E. RYAN JR.², S. H. COHEN³, R. A. WINDHORST^{3,2}, AND I. WADDINGTON⁴

Draft version October 31, 2018

ABSTRACT

We report on a statistical study of the 51 radio galaxies at the millijansky flux level from the Faint Images of the Radio Sky at Twenty centimeters, including their optical morphologies and structure obtained with the Hubble Space Telescope. Our optical imaging is significantly deeper (~ 2 mag) than previous studies with the superior angular resolution of space-based imaging. We find 8/51 (16%) of the radio sources have no optically identifiable counterpart to $AB \sim 24$ mag. For the remaining 43 sources, only 25 are sufficiently resolved in the HST images to reliably assign a visual classification: 15 (60%) are elliptical galaxies, 2 (8%) are late-type spiral galaxies, 1 (4%) is an S0, 3 (12%) are point-like objects (quasars), and 4 (16%) are merger systems. We find a similar distribution of optical types with measurements of the Sérsic index. The optical magnitude distribution of these galaxies peaks at $I \simeq 20.7 \pm 0.5$ AB mag, which is ~ 3 mag brighter than the depth of our typical HST field and is thus not due to the WFPC2 detection limit. This supports the luminosity-dependent density evolutionary model, where the majority of faint radio galaxies typically have L^* -optical luminosities and a median redshift of $z \simeq 0.8$ with a relatively abrupt redshift cut-off at $z \gtrsim 2$. We discuss our results in the context of the evolution of elliptical galaxies and active galactic nuclei.

Subject headings: galaxies: starburst — radio continuum: galaxies

1. INTRODUCTION

Faint radio galaxies are good probes of typical galaxies at large distances since they lack a significant contribution from non-thermal light or strong emission lines in their optical spectra (eg. Kron, Koo, & Windhorst 1985; Benn et al. 1993; Hammer et al. 1995a). Furthermore, their selection is relatively unaffected by dust absorption when these galaxies are identified by their synchrotron emission. In the local Universe, powerful radio sources are primarily found in giant elliptical galaxies, which suggests that radio selection may be an efficient method of identifying high-redshift ellipticals. However, at lower radio powers, typically below the break in the radio luminosity function, there is an increasing fraction of star-forming and active galaxies (such as Seyferts and LINERS; eg. Condon 1989; Benn et al. 1993; Lowenthal 1997; Hopkins et al. 2003; Best et al. 2005; Afonso et al. 2006; Mainieri et al. 2008). Often of the galaxy identification is not based on deep, high-resolution optical imaging, but rather on broadband optical colors. Such classification schemes are only reliable to the extent to which these colors directly map onto the Hubble sequence at a given redshift. Therefore, in this paper we focus on the optical morphologies and structure of radio galaxies with fluxes of $1 \text{ mJy} \lesssim S_{1.4 \text{ GHz}} \lesssim 100 \text{ mJy}$ (we will denote $S_{1.4}$ as

integrated radio flux at 1.4 GHz throughout) obtained from the Hubble Space Telescope (HST).

Early studies indicate that the majority of millijansky radio galaxies typically have extended radio emission with optical colors and luminosities comparable to local elliptical galaxies (Kron, Koo, & Windhorst 1985; Windhorst et al. 1985; Benn et al. 1993; Hammer et al. 1995a). The remainder of these radio sources are generally quasars or very blue galaxies, which are often interpreted as late-type, starburst systems. Like the most powerful radio sources, millijansky galaxies have a broad redshift distribution of $0 \lesssim z \lesssim 1.5$ (Overzier et al. 2003), which reflect the increase of active galaxies and radio emission from $z \sim 0$ to $z \sim 2$ (eg. Hopkins & Beacom 2006). The space density of millijansky radio galaxies evolves strongly with redshift, which can be reproduced by a simple evolutionary model. Condon (1989) argue that the majority of these radio galaxies reside in a “shell” of radius $z \sim 0.8$ with thickness of $\delta z \sim 0.8$. In addition to supporting this model, Waddington et al. (2001) find a deficit of high redshift ($z \gtrsim 2$) millijansky radio galaxies in the Hercules field of the Leiden-Berkley Deep Survey (LBDS). They interpret this result as an effective redshift “cut-off,” which varies from $z \simeq 2$ for the most luminous radio sources, to $z \simeq 1$ for the lower luminosity galaxies.

Millijansky radio sources are intrinsically rather luminous at optical wavelengths, with absolute magnitudes in a relatively narrow range (± 0.8 mag) centered at $M_{r^*} \simeq -22$ mag and $M_{r^*} \simeq -23$ mag for blue and red galaxies, respectively (Machalski & Godlowski 2000; Ivezić et al. 2002). From photographic plate and deep CCD imaging, Windhorst et al. (1984b) and Waddington et al. (2000) found that the apparent magnitude distribution from the LBDS peaks around $I \simeq 22$ mag, which at $z = 0.8$ corresponds to $M_B \simeq -21.5$ mag. While there is a good deal of deep ground-based imaging on mil-

*BASED ON OBSERVATIONS MADE WITH THE NASA/ESA HUBBLE SPACE TELESCOPE, OBTAINED FROM THE DATA ARCHIVE AT THE SPACE TELESCOPE SCIENCE INSTITUTE, WHICH IS OPERATED BY THE ASSOCIATION OF UNIVERSITIES FOR RESEARCH IN ASTRONOMY, INC., UNDER NASA CONTRACT NAS 5-26555.

² Dept. of Physics, Arizona State University, Tempe, AZ 85287-1504, USA

³ School of Earth and Space Exploration, Arizona State University, Tempe, AZ 85287-1404, USA

⁴ Astronomy Centre, University of Sussex, Brighton, BN1 9QH, UK

Electronic address: jq@asu.edu

lijansky radio sources, there is little high-resolution HST imaging. Early works with HST are generally based on at most a few objects (Pascarelle et al. 1996; Waddington et al. 1999, 2002).

In the microjansky flux range, Afonso et al. (2006) identified 64 faint radio galaxies of which 57 had optical counterparts in the Advanced Camera for Surveys (ACS) imaging of the Great Observatories Origins Deep Survey, South (GOODS-S; Giavalisco et al. 2004). The median photometric redshift of the optically identified microjansky radio sources is also $z \sim 0.8$. Since the redshift distribution of radio galaxies changes only very slowly for radio fluxes below $S_{1.4} \simeq 1$ Jy (Windhorst et al. 1990), this median photometric redshift is consistent with the evolutionary model of Condon (1989). Based on their X -ray properties and limited optical spectroscopy, the majority of these microjansky radio galaxies are either active galactic nuclei (AGN) or star-forming galaxies (Afonso et al. 2006). Furthermore, the optical counterparts generally have disturbed morphologies, which suggests many are in the later stages of merging.

In this paper, we investigate the optical properties of millijansky radio galaxies selected from the Faint Images of the Radio Sky at Twenty centimeters (FIRST; Becker et al. 1995). The FIRST survey covers $\simeq 10^4$ square degrees of the north Galactic cap to a 95% completeness limit of $\simeq 2.8$ mJy. In order to reliably determine the morphology of these small and faint optical counterparts, we require the angular resolution of space-based imaging. Therefore, our sample is derived from the overlap of FIRST sources with the existing HST-WFPC2 Archive as of 2002. All magnitudes quoted herein are in the AB system (Oke & Gunn 1983). This paper is organized as follows: In § 2 we outline the critical steps to define our final millijansky sample, in § 3 we discuss our four primary results, in § 4 we provide general comments on individual objects, and in § 5 we conclude with a general summary and additional discussion of our results.

2. PROCEDURE

2.1. Data Selection

We begin by correlating the positions from the FIRST catalog with the HST-WFPC2 Archive. Out of $\gtrsim 10^4$ WFPC2 images, we obtain ~ 850 potential frames with FIRST sources. These WFPC2 images were stacked and cosmic-ray cleaned following the method discussed by Cohen et al. (2003) to yield a sample of 177 optical candidates. The HST-WFPC2 dataset contains all the archival F606W (V) and F814W (I) images with exposure times longer than 160 seconds, however only a single band is generally available for a given target, as the primary goals of the HST images. Roughly 50% of the WFPC2 data are observed as HST parallel fields, which are images taken by WFPC2 when a different instrument was observing the primary target. In general, these millijansky radio sources are extremely difficult to image since they are typically optically faint ($I \gtrsim 20$ mag) and distributed over degree scales. Therefore, these parallel observations provide an efficient method to optically image this elusive population.

2.2. Secondary Selection Criteria

Since the motivation of this work is to study the optical morphologies and structure of a well defined, *ran-*

TABLE 1
SAMPLE REDUCTION SUMMARY

Reason	Number
Radio Sources In Final Sample	51
Excluded because of Pointed HST Observations	43
Excluded because NGC or Nearby Contamination	32
Excluded because Incomplete in Radio Flux Cutoff	47
Misc ^a	4
Total	177

^aThis category includes fields where the target is uncertain due to a galaxy group or cluster, saturated WFPC2 fields, and/or local WFPC2 defects precluding inclusion in the optical sample.

dom, and complete sample of weak radio galaxies with the superior resolution of HST, many of the candidates must be eliminated from the sample. There are four reasons what we could exclude a given field: (1) Major WFPC2 image defects, such the majority of the pixels are saturated from nearby stars; (2) a significant fraction of the field-of-view is covered by a nearby object, such as an NGC-type galaxy, which would prevent reliable optical flux measurements and morphological classifications; (3) the WFPC2 image was centered on a dense star-field or galaxy cluster to eliminate ambiguity in the optical identifications; or (4) the radio source was *targeted* by HST. In this way, we can subselect a complete sample of background objects from a non-random set of foreground observations. Furthermore, owing to the relatively small WFPC2 field-of-view, most FIRST radio sources are generally the primary target. In Table 1, we summarize the eliminated fields. The selection effects of the various HST programs is not always possible to quantify based on the HST target lists and PI proposals available in the STScI/HST Archive. In Table 2, we list the targeted radio sources that were removed to reduce the contamination of preselected objects in constructing our random sample. These criteria provide a compromise between the resulting completeness and reliability of the final sample. The majority of the radio sources are brighter than the 95% completeness limit of the FIRST survey of $S_{1.4} \simeq 2.8$ mJy. From the 177 FIRST candidates, our final sample contains 51 radio galaxies with HST-WFPC2 observations.

2.3. Astrometric Correction of HST Fields

Due to technical issues in the the world coordinate system (WCS) generated in the HST-WFPC2 pipeline, the astrometry keywords in the FITS headers of WFPC2 fields prior to 1997 September 15 may be unreliable (Biretta et al. 2000). To better calibrate the astrometry of these frames, we match the objects in each field with the United States Naval Observatory (USNO) A2.0 catalog (Monet et al. 1996), which is the standard in the FK5 system. We derive shifts in Right Ascension ($\Delta\alpha$) and Declination ($\Delta\delta$) from the positional differences between the HST-WFPC2 images and USNO catalog, which we show in Figure 1. These offsets are individually applied to their respective WFPC2 frame. However, several fields lacked usable USNO sources, and were left uncorrected. In general, these were high-latitude fields or contained only saturated stars, which made accurate determination of their centers unreliable. While the dispersion in $\Delta\delta$ is not significantly higher for the pre-1997 data, it

TABLE 2
TARGETED SOURCES REMOVED FROM SAMPLE

Radio Source ^a	RA J2000 (deg)	Dec J2000 (deg)	$\log S_{1.4}$ (mJy)	WFPC2 Target (targname) ^b
J001303.7-012305	3.265625	-1.384777	0.61	CL-ULIR00105-0139
J022448.1-000711	36.200542	-0.120111	0.04	GAL-CLUS-022448-000717
J074123.0+320810	115.345963	32.136360	0.60	QDOTULIR073810+321511
J082209.5+470552	125.539925	47.098114	1.72	A646
J082313.7+275120	125.807213	27.856083	1.03	QDOTULIR082010+280119
J083803.6+505509	129.515091	50.919613	0.88	QDOTULIR0838+5055
J090850.9+374818	137.211304	37.805500	3.06	3C217
J094308.4+465700	145.785828	46.950359	0.20	GAL-CLUS-093942+47
J095254.3+435348	148.226196	43.896782	0.85	GAL-CLUS-0952+44
J095644.7+493034	149.187088	49.513168	0.68	A895
J102326.2+124855	155.859283	12.815556	0.22	ABELL999-BCG
J103141.7+350231	157.924042	35.044613	1.64	A1033
J105648.8-033727	164.203873	-3.623805	0.82	GAL-CLUS-105427-032125-POS1
J105659.5-033727	164.248123	-3.624416	1.09	GAL-CLUS-105427-032125-POS5
J110050.3+104654	165.211929	10.783639	1.06	AO1058+11
J115106.8+550443	177.778549	55.078945	0.95	UGC06823
J122906.7+020308	187.277954	2.052416	4.57	PG1226+023
J123357.1+074206	188.488297	7.701722	0.87	NGC4526
J125929.2+361713	194.875290	36.284283	2.17	6C1257+36
J131128.9-012116	197.870880	-1.354444	0.36	ABELL1689
J131130.0-012028	197.875122	-1.341333	0.94	A1689-10
J131131.5-011931	197.880920	-1.325666	1.63	ABELL1689
J131132.6-011959	197.886169	-1.333000	0.39	A1689-10
J133238.3+503335	203.159988	50.560001	0.78	A1758G7
J133239.4+503432	203.164673	50.575615	0.77	A1758G7
J133557.2+544338	203.987244	54.726387	1.09	MS1333.9+5500
J134337.1-001525	205.904648	-0.257166	0.74	GAL-CLUS-134339-001349
J134447.4+555410	206.197723	55.903053	0.10	IR13428+5608.0
J134733.3+121724	206.889297	12.290195	3.69	PKS1345+12-PSF
J135609.9+290535	209.041580	29.093473	1.03	NGWULIR1353+2920
J140318.1+542157	210.824783	54.365974	1.14	NGC5457-FLD1
J141721.3+132429	214.339127	13.408417	0.37	MS1414.9+1337
J142357.6+383247	215.990982	38.546196	1.02	FSC142118+3845
J142553.5+374805	216.473129	37.801472	0.27	A1914
J143242.8+245614	218.172867	24.921638	2.09	B2+1430+25
J144516.4+095836	221.318619	9.976666	3.38	1442+101
J151002.9+570243	227.512466	57.045555	2.41	GB1508+5714
J160218.2+155912	240.576035	15.986777	0.87	ABELL2147-BCG
J162124.6+381008	245.353226	38.169422	0.75	R1621+38
J162439.6+234524	246.162979	23.753334	3.15	GAL-CLUS-3C336-POS2
J162548.7+264658	246.453186	26.782833	0.99	Q1623+268
J164658.9+454824	251.745468	45.806778	0.74	QDOTULIR1645+4553
J231713.1-110034	349.305084	-11.009694	0.82	CL-ULIR23146-1117

^aThe name of the source as per IAU recommendations, as used by FIRST. FIRST Jhhmmss.s+ddmmss in which the coordinates are equinox J2000.0 and are truncated (Becker et al. 1995).

^bThis is the header keyword for the field target from the WFPC2 images.

does increase by a factor of ~ 4 for the dispersion in $\Delta\alpha$. The applied shifts roughly follow a normal distribution centered on $\langle(\Delta\alpha, \Delta\delta)\rangle = (-0''.1, 0''.0)$ with standard deviations of $(\sigma_{\alpha}^{\text{opt}}, \sigma_{\delta}^{\text{opt}}) = (0''.85, 0''.55)$. This mean offset gives a systematic uncertainty of $\simeq 0''.1$, while the 1σ random uncertainty is $\simeq 1''.0$.

2.4. WFPC2 Image Preparation and Investigation

We excise 300×300 pixel ‘‘postage stamp’’ images from the astrometrically corrected and stacked WFPC2 mosaics centered on each FIRST source position. In Figure 2, we show the 51 WFPC2 stamps with FIRST radio contours placed at 2^n multiples of 0.31 mJy, and list the relevant photometric and morphological information

in the upper-left corner. Optical counterparts to the given radio sources are identified by the spatial alignment between the optical image and the center of the radio contours. Since several objects have complex radio morphologies (such as elongated or double isophotes), the identification of each most likely optical counterpart was for such objects done on a case-by-case basis. For the FIRST sources with a double-lobed morphology, we adopt the optical object which is nearest to the geometric center of the lobes as the most likely identification (eg. Mackay 1971). If the optical counterpart is considerably off the line which connects the two lobes, then we use the the orientation and outer isophotes to aide in the identification (such as in the case of J094930.7+295938).

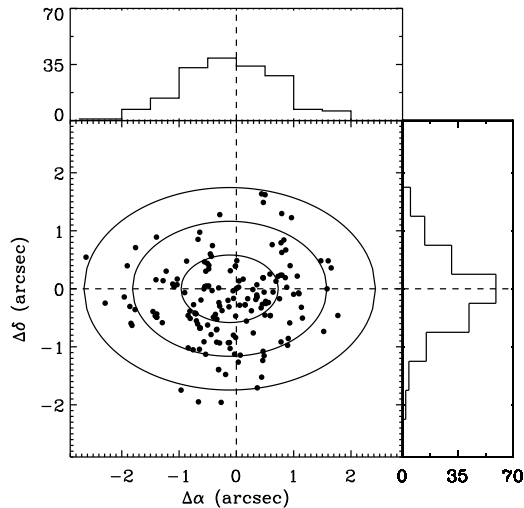


FIG. 1.— Optical astrometric corrections in RA and Dec. These relative offsets are computed as the positional difference between the HST-WFPC2 and USNO coordinates for multiple stars in a given field. Both distributions are roughly Gaussian with mean values of $(\Delta\alpha, \Delta\delta) = (0''.1, 0''.0)$, with standard deviations $(\sigma_{\alpha}^{\text{opt}}, \sigma_{\delta}^{\text{opt}}) = (0''.85, 0''.55)$. The ellipses represent the 1σ , 2σ , and 3σ contours. These systematic offsets and uncertainties are used to determine the most likely optical identification for radio galaxies discussed in § 2.4.

TABLE 3
UNIDENTIFIED RADIO SOURCES

Radio Source ^a	Passband	Limit ^b (mag)	$\log S_{1.4}$ (mJy)
J030237.6+000818	F814W	24.5	0.70
J082828.4+344131	F814W	24.7	1.01
J120326.4+443635	F606W	25.0	1.43
J121839.7+295325	F606W	24.8	1.53
J125635.3+215632	F814W	24.2	0.52
J150109.7+225111	F814W	23.6	0.82
J151057.4+312722	F606W	23.7	0.49
J164911.4+305226	F606W	24.3	0.44

^aThe name of the source as per IAU recommendations, as used by FIRST. FIRST Jhhmmss.s+ddmmss in which the coordinates are equinox J2000.0 and are truncated (Becker et al. 1995).

^bThe limiting AB magnitude in specified filter given as 50% completeness limit following Snigula et al. (2002).

Both lobes of double radio sources are confirmed to not separately contain optical counterparts. Stamps with no optical object within the radio contours (complete to 2.8 mJy) were deemed *unidentified* radio sources (hereafter, Unid) to the limiting optical magnitude cataloged in Table 3. For identified optical counterparts, we assign visual types and measure their surface brightness profiles (see § 3.1), however the faintest and smallest HST objects are generally not classifiable (Odewahn et al. 1996; Cohen et al. 2003).

To quantify the reliability of the radio-optical identification, we use the likelihood ratio (LR) technique described by de Ruiter et al. (1977). If we assume that the optical and radio sources are intrinsically located at the same position, and that potential clustering does not lead to a large fraction of false identifications, then the likelihood that a radio source and its potential identification

are the same physical object can be defined as:

$$LR(r) = \frac{1}{2\lambda} \exp\left(\frac{r^2(2\lambda - 1)}{2}\right), \quad (1)$$

where

$$r = \sqrt{\left(\frac{\alpha^{\text{rad}} - \alpha^{\text{opt}}}{\sigma_{\alpha}}\right)^2 + \left(\frac{\delta^{\text{rad}} - \delta^{\text{opt}}}{\sigma_{\delta}}\right)^2}, \quad (2)$$

$$\lambda = \pi\sigma_{\alpha}\sigma_{\delta}\rho_{BG}, \quad (3)$$

$$\sigma_{\alpha} = \sqrt{(\sigma_{\alpha}^{\text{rad}})^2 + (\sigma_{\alpha}^{\text{opt}})^2}, \quad (4)$$

$$\sigma_{\delta} = \sqrt{(\sigma_{\delta}^{\text{rad}})^2 + (\sigma_{\delta}^{\text{opt}})^2}. \quad (5)$$

where ρ_{BG} is the surface density of objects, $(\sigma_{\alpha}^{\text{rad}}, \sigma_{\delta}^{\text{rad}})$ are the radio positional uncertainties (Becker et al. 1995), $(\sigma_{\alpha}^{\text{opt}}, \sigma_{\delta}^{\text{opt}})$ are the uncertainties in the WCS shifts derived from the fits headers (discussed in § 2.3 and Figure 1), and $(\alpha^{\text{rad}}, \delta^{\text{rad}})$ and $(\alpha^{\text{opt}}, \delta^{\text{opt}})$ are the celestial coordinates of the radio and optical sources, respectively.

In these relatively shallow and narrow HST fields, an accurate background density of objects cannot always be determined. Therefore, we adopt the method of Snigula et al. (2002) to estimate the galaxy flux at the 50% completeness limit. This flux is found by assuming a given light-profile, and using the noise properties of the image to determine the brightness limit to which 50% the objects would have been recovered. For a given total magnitude, pure disk galaxies have a lower surface brightness than pure ellipticals, and are therefore somewhat more difficult to detect. However, the 50% completeness limit for an exponential and de Vaucouleurs typically differ by only $\lesssim 0.1$ mag for a fixed size of $r = 0''.3$ (Cohen et al. 2003). Given this minor difference in brightness for the two light-profiles, we adopt the limits derived from the de Vaucouleurs profile, which are given in Table 4. Finally, we integrate the observed I -band number counts (Metcalf et al. 1996; Odewahn et al. 1996; Casertano et al. 2000; Gardner & Satyapal 2000; Yasuda et al. 2001) to these derived limits to determine the background density (ρ_{BG}) in equation (3).

The resulting likelihood ratios are listed in Table 4, and their distribution is plotted in Figure 3. Following de Ruiter et al. (1977), a $LR \geq 2$ provides a compromise between reliability and completeness for the radio-optical identifications. Therefore, we adopt the de Ruiter et al. (1977) likelihood threshold, where objects with $LR \geq 2$ are a positive identification. For radio sources with no obvious counterpart (the Unids), the likelihood ratio was computed for the nearest optical source, and all of these systems have a $LR \ll 2$.

3. RESULTS

3.1. Optical Morphologies

Many of the counterparts to these faint radio galaxies are also very faint in the optical. Only 2/43 galaxies have $I \lesssim 16.0$ mag, the approximate brightness limit to classify galaxies from ground-based imaging in average seeing conditions. Of the 43 radio sources for which an optical counterpart was found, only 25 can be visually classified to a brightness limit of $AB \lesssim 22$ mag. The visual morphologies were determined by three independent observers (J.R., S.H.C., and R.A.W.), and the average

TABLE 4
FLUX RESULTS

Radio Source ^a	Band ^b	Magnitude (mag)	SB ^c (mag/□′′)	log $S_{1.4}$ ^d (mJy)	Depth ^e (mag)	LR ^f	i' ^g (mag)	$(g' - r')$ ^g (mag)	$(r' - i')$ ^g (mag)
J002219.1–013030	V	24.59	23.39	0.47	25.2	11.17
J004322.3–001343	V	18.93	16.12	0.83	23.9	10.17	18.91±0.02	0.28±0.02	0.12±0.03
J012616.6–012126	V	19.84	22.45	1.15	23.9	2.03
J030237.6+000818	I	0.70	24.5	0.0
J030249.5+000615	I	19.79	20.33	0.15	24.7	6.42	20.13±0.18	0.64±0.27	0.65±0.22
J082820.6+344321	I	25.59	27.21	0.69	24.9	11.65
J082828.4+344131	I	1.01	24.7	0.0
J084715.5+443752	I	24.66	23.27	0.62	23.5	44.39
J084849.5+445550	I	19.29	21.06	0.67	24.6	10.53	19.13±0.06	2.40±0.61	1.02±0.12
J091205.2+350506	V	23.79	22.50	0.93	23.7	17.04
J091251.0+525928	I	21.14	20.80	0.47	22.9	23.59	20.42±0.12	4.79±0.89	1.51±0.34
J094926.6+295941	V	20.06	21.85	1.25	25.4	8.43	19.14±0.07	2.08±0.28	0.64±0.12
J094930.7+295938	V	22.70	22.54	0.55	25.6	3.87
J100354.5+285911	V	23.10	24.77	0.60	24.6	6.25	22.44±0.44	0.96±1.45	1.70±1.07
J102437.2+470312	I	21.75	20.36	0.39	24.3	15.62	22.31±0.31	1.36±0.78	0.91±0.49
J102744.6+282921	I	22.44	24.31	0.15	24.6	13.33
J103452.3+394704	I	21.73	21.94	1.40	24.5	27.44	21.82±0.48	1.92±1.26	0.39±0.63
J104630.8–001213	I	18.8	21.73	0.65	24.0	28.24	19.19±0.08	1.91±0.29	0.71±0.13
J104757.0+123835	V	20.61	20.77	0.94	24.2	22.27	19.33±0.06	2.04±0.31	0.77±0.09
J111908.6+211917	V	15.79	16.85	0.71	24.2	6.92	14.15±0.00	−0.08±0.00	0.35±0.00
J112520.7+420425	I	19.36	20.67	0.28	24.2	21.47	19.54±0.06	1.76±0.45	1.21±0.14
J114526.3+193301	V	24.40	22.67	0.84	24.8	12.83	22.79±0.36	0.30±0.66	0.88±0.65
J114910.5–002313	V	22.82	23.44	0.75	23.3	20.46	22.62±0.95	3.97±1.13	0.41±1.30
J114928.3+143844	V	22.83	20.71	1.15	24.5	25.49
J115642.8+022451	V	18.99	20.42	1.00	18.21±0.02	1.09±0.03	0.32±0.03
	I	17.81	18.02	1.00	24.3	10.35	18.21±0.02	1.09±0.03	0.32±0.03
J120326.4+443635	V	1.43	25.0	0.0
J121026.6+392909	V	19.53	16.29	1.27	25.0	12.55	18.98±0.02	0.34±0.03	0.45±0.03
J121658.4+375439	I	20.56	19.36	0.41	23.3	20.20
J121705.5–031137	I	23.89	22.49	1.51	24.3	11.34
J121707.7–031127	I	15.67	17.34	0.97	23.2	2.44
J121839.7+295325	V	1.53	24.8	0.0
J122331.0+155245	I	21.02	19.03	0.64	24.9	18.67	23.91±2.84	0.92±0.77	−1.66±2.87
J122624.4+173228	V	18.82	20.38	1.15	24.5	13.56
J125029.2+302527	I	17.83	19.93	0.44	23.9	31.38	17.85±0.02	1.34±0.04	0.53±0.03
J125635.3+215632	I	0.52	24.2	0.0
J125650.0+220630	V	22.44	20.71	0.83	24.7	5.71
J131223.6+424517	I	23.19	22.90	0.47	25.9	8.08
J131617.8+420239	V	16.66	19.42	0.00	24.3	14.92	16.12±0.01	0.78±0.01	0.45±0.01
J134219.9–005816	I	24.08	23.53	1.23	24.0	17.42
J140019.9+044421	I	19.51	20.32	0.05	24.6	9.73	19.51±0.10	1.47±0.43	1.08±0.22
J143530.0+484534	V	22.07	23.13	0.94	24.3	17.58
J150109.7+225111	I	0.82	23.6	0.0
J151057.4+312722	V	0.49	23.7	0.0
J153955.0+342013	V	19.49	21.28	1.11	23.7	26.62	18.21±0.04	1.86±0.12	0.58±0.06
J155938.7+473309	V	25.37	24.08	0.49	25.0	6.78
J163141.4+373603	V	19.87	20.87	0.41	24.7	6.43	18.57±0.05	1.62±0.17	0.81±0.08
J163233.8+190550	I	22.36	21.26	0.26	23.4	17.40
J164911.4+305226	V	0.44	24.3	0.0
J171901.1+480458	V	21.01	21.27	0.34
	I	19.57	19.57	0.34	23.9	11.65
J172025.4+480321	V	21.66	22.43	1.48	23.1	75.08
J172232.9+501232	V	20.11	20.65	0.45
	I	18.56	19.44	0.45	24.4	9.80

^aThe name of the source as per IAU recommendations, as used by FIRST. FIRST Jhhmmss.s+ddmmss in which the coordinates are equinox J2000.0 and are truncated (Becker et al. 1995).

^bV and I refer to the HST-WFPC2 bandpasses F606W or F814W, respectively.

^cSurface brightness in mag/arcsec² within the effective radius (R_e).

^dIntegrated flux at 1.4 GHz in mJy provided by the FIRST catalog.

^eThe 50% completeness limit as determined by the Snigula et al. (2002) method (see § 2.4).

^fThe likelihood ratio as discussed § 2.4.

^gObtained from SDSS-dr5 (Adelman-McCarthy et al. 2007).

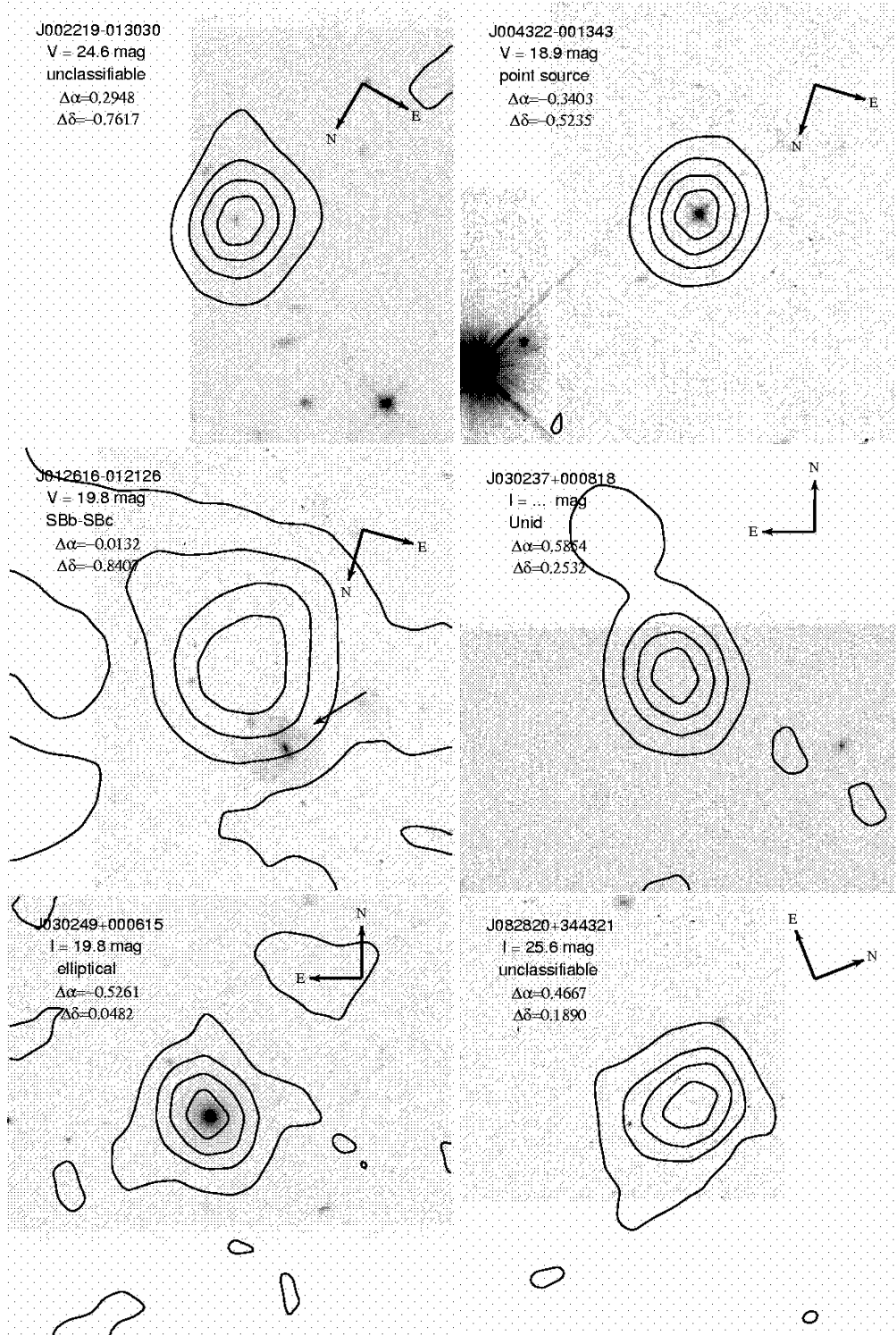
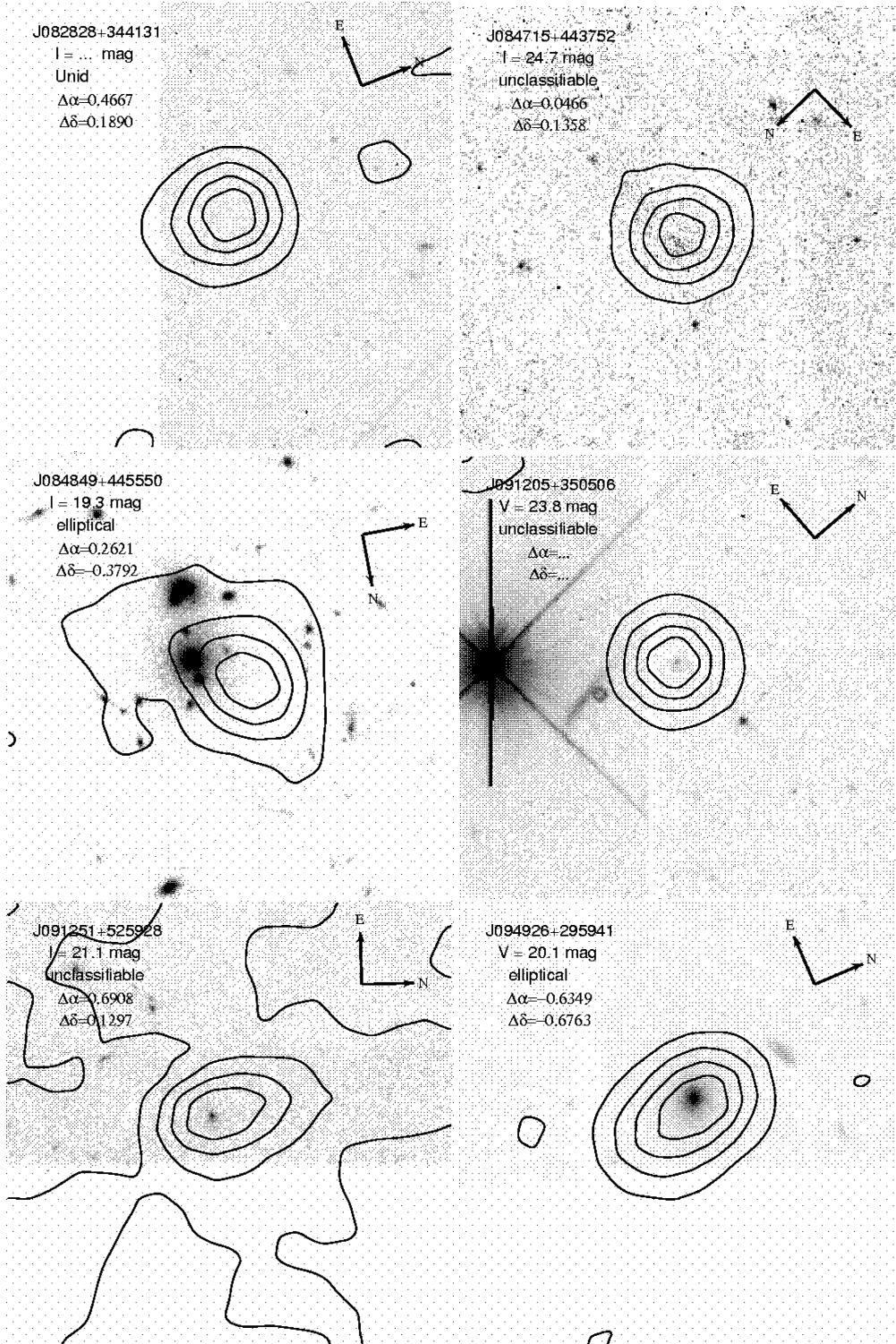


FIG. 2.— WFPC2 images of our 60 millijansky radio sources. Objects not located in the middle of the radio contours are indicated by an arrow. In the upper left of each stamp, we list the name from the FIRST catalog, the HST-WFPC2 optical magnitude in the given bandpass, the visually-defined morphology, and shifts in RA and Dec ($\Delta\alpha$ and $\Delta\delta$) defined in § 2.3. Each stamp is $30'' \times 30''$. **Higher resolution images are available by request.**



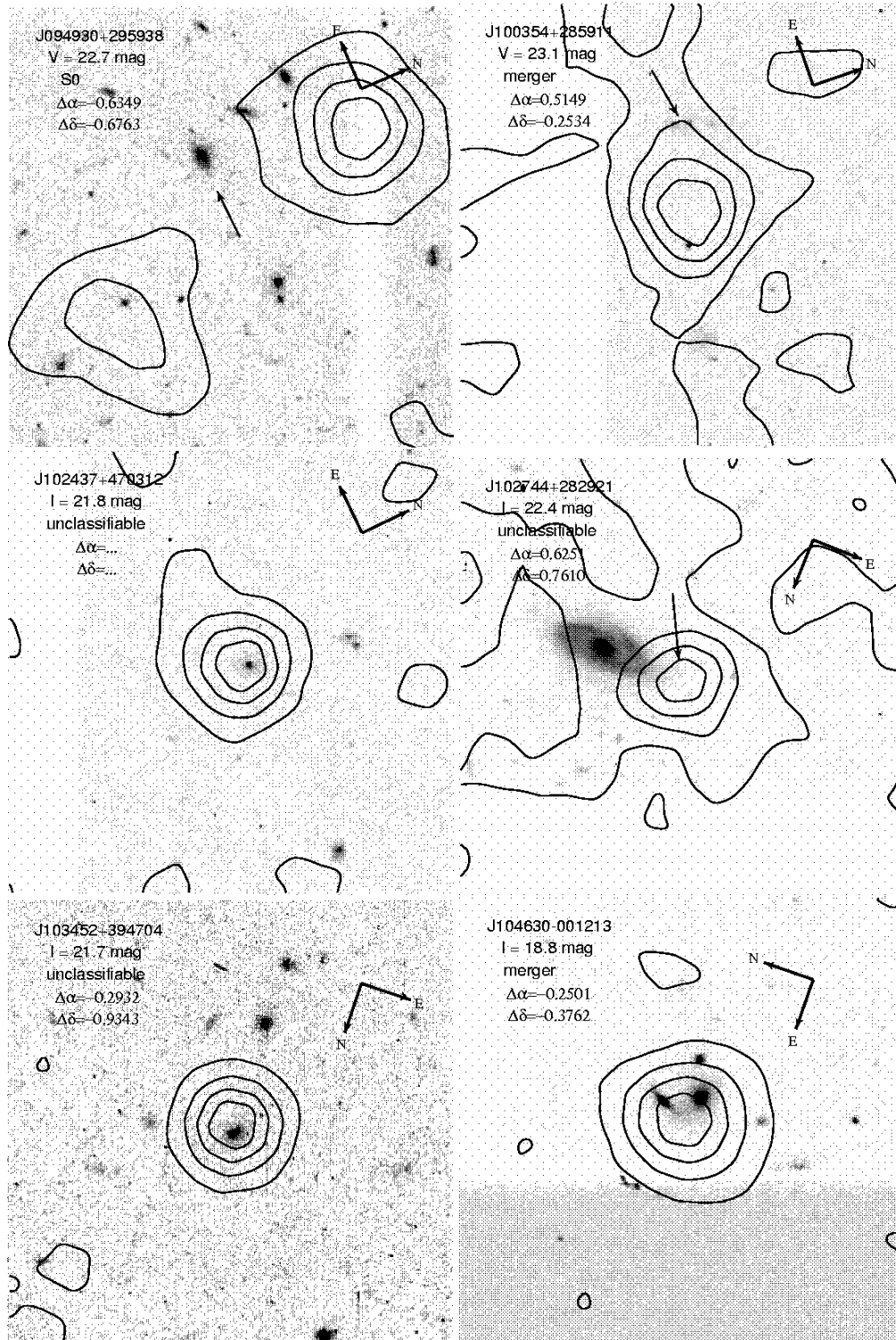
classification is listed for each object in Table 5. In order to also provide some *quantitative* measure of the galaxy morphologies, we fit the surface-brightness profiles with the Sérsic or $r^{1/n}$ of model:

$$I(r) = I_e \exp \left(-b_n \left[\left(\frac{r}{r_e} \right)^{1/n} - 1 \right] \right), \quad (6)$$

where I_e is the intensity at the effective radius r_e and b_n is a constant defined in terms of n which describes the shape of the profile (eg. Graham & Driver 2005). The Sérsic index (n) can morphologically classify galaxies by

type, where elliptical galaxies have $n \simeq 4$ and later-type disk galaxies have $n \simeq 1$. Therefore, we have a quantitative, morphological measurements to complement our visual classifications for the 25/43 classifiable, optical counterparts. We give these results in Table 5.

For the 25/43 galaxies which are sufficiently bright and extended to be visually classified, there are 15 ellipticals, 1 S0, 2 late-type spirals, 3 optical point sources (these are generally quasars, see § 4), and 4 mergers. Therefore, at the millijansky flux levels, 19/25 galaxies are early-type or quasars, while only 2/25 are later-type galaxies.



However, the surface brightness analysis permits a “continuum” of galaxy types based on the best-fit value for the Sérsic index. Therefore, to produce a comparable classification scheme (such as early- versus late-type), we collapse this continuum using a threshold value for the Sérsic index of $n \geq 2$ are early-types and $n < 2$ are late-types (eg. Driver et al. 2006). Of the 34/43 galaxies for which we could reliably measure the Sérsic index, 20 are early-types while 14 are later-types, and seven of these only have $n < 2$ at the 1σ -level (such as J002219.1–013030). Based on these Sérsic indices, we find $\sim 60\%$ of

millijansky radio galaxies are morphologically early-type systems. Furthermore, these classifications based on the Sérsic index generally agree with our visually assigned morphologies. Based on these morphological analyses, the dominance of red galaxies in millijansky radio galaxy samples (Kron, Koo, & Windhorst 1985; Hammer et al. 1995a) is now confirmed by robust morphological observations with high-resolution imaging from HST.

TABLE 5
MORPHOLOGICAL AND STRUCTURAL RESULTS

Radio Source ^a	R_e^b (arcsec)	n^c	χ_ν^{2d}	ANN ^e Type	Visual ^f Type	WFPC2 ^g Target
J002219.1–013030	0.23	1.56±0.82	0.30	2.5	x	ANY
J004322.3–001343	0.11	–4.1	ps	ANY
J012616.6–012126	1.33	4.95±0.74	0.11	5.0	SBb-SBc	ANY
J030237.6+000818	UNID	FIELD-030239+00065
J030249.5+000615	0.51	4.39±0.41	0.01	–2.3	E	FIELD-030251+00071
J082820.6+344321	0.84	5.5	x	6C0825+34
J082828.4+344131	UNID	6C0825+34
J084715.5+443752	0.21	1.00±0.00	1.84	8.5	xE	GAL-084720+443739
J084849.5+445550	0.90	3.98±0.03	0.19	0.6	E (cluster)	LYNX-E
J091205.2+350506	0.22	1.24±0.75	0.05	7.6	xE	ANY
J091251.0+525928	0.34	1.80±0.70	0.18	5.2	xE	SBS0909+523
J094926.6+295941	0.91	3.46±0.46	0.01	–3.1	E	ANY
J094930.7+295938	0.37	2.00±0.54	0.02	1.1	S0	ANY
J100354.5+285911	0.86	7.2	merger	ANY
J102437.2+470312	0.21	3.77±0.02	1.19	–4.1	xE	PAR
J102744.6+282921	0.94	6.8	x	HIGH
J103452.3+394704	0.44	2.66±0.67	0.20	2.1	xE	PAR
J104630.8–001213	1.57	3.0	merger	10HR-B
J104757.0+123835	0.43	2.58±0.41	0.01	–2.5	E	ANY
J111908.6+211917	0.65	2.63±0.23	0.11	–0.9	ps	PG1116+215
J112520.7+420425	0.73	1.72±0.44	0.01	3.0	E/S0	HI-LAT
J114526.3+193301	0.18	0.73±0.24	1.08	3.0	xC	ANY
J114910.5–002313	0.53	3.66±0.04	0.50	8.3	xC	ANY
J114928.3+143844	0.15	2.17±0.30	0.25	0.9	E	ANY
J115642.8+022451	0.44	1.76±0.60	0.04	1.9	E	PAR
J120326.4+443635	UNID	ANY
J121026.6+392909	0.09	4.28±0.02	0.73	–2.8	ps	ANY
J121658.4+375439	0.23	5.45±0.33	0.06	–2.6	xE	MS1214.3+3811
J121705.5–031137	0.21	0.50±0.17	0.00	6.4	x	2MASSW-J1217-03
J121707.7–031127	0.86	2.62±0.39	0.03	–3.5	E	2MASSW-J1217-03
J121839.7+295325	UNID	ANY
J122331.0+155245	0.16	–1.7	xC	PAR
J122624.4+173228	0.82	3.08±0.39	0.04	–2.2	E (companion)	ANY
J125029.2+302527	1.05	1.96±0.48	0.09	0.4	E (companions)	HI-LAT
J125635.3+215632	UNID	ANYWHERE
J125650.0+220630	0.18	3.81±0.07	1.88	–1.2	xC	ANY
J131223.6+424517	0.35	1.54±0.70	0.10	3.1	E	SSA13E
J131617.8+420239	1.42	1.48±0.34	0.54	0.2	SBc	ANY
J134219.9–005816	0.31	8.8	x	HI-LAT
J140019.9+044421	0.58	5.43±0.33	0.06	–0.5	E (companions)	BIG2
J143530.0+484534	0.65	6.4	merger	NGC5689
J150109.7+225111	UNID	TVLM513-46546
J151057.4+312722	UNID	WAS96
J153955.0+342013	0.91	2.68±0.54	0.01	3.6	E	ANY
J155938.7+473309	0.22	0.47±0.19	0.86	8.6	xC	ANY
J163141.4+373603	0.63	2.81±0.41	0.04	–3.3	E	PAR
J163233.8+190550	0.24	1.88±1.72	0.03	3.4	xC	2MASSW1632+1904
J164911.4+305226	UNID	HIGH
J171901.1+480458	0.40	3.10±0.51	0.01	–0.8	E	HIGH
J172025.4+480321	0.57	0.68±0.28	0.26	6.1	xE	ANY
J172232.9+501232	0.60	–2.3	merger	PAR

^aThe name of the source as per IAU recommendations, as used by FIRST. FIRST Jhhmmss.s+ddmmss in which the coordinates are equinox J2000.0 and are truncated (Becker et al. 1995).

^bHalf light radius in arcsec as measured by LMORPHO (Odewahn et al. 1996).

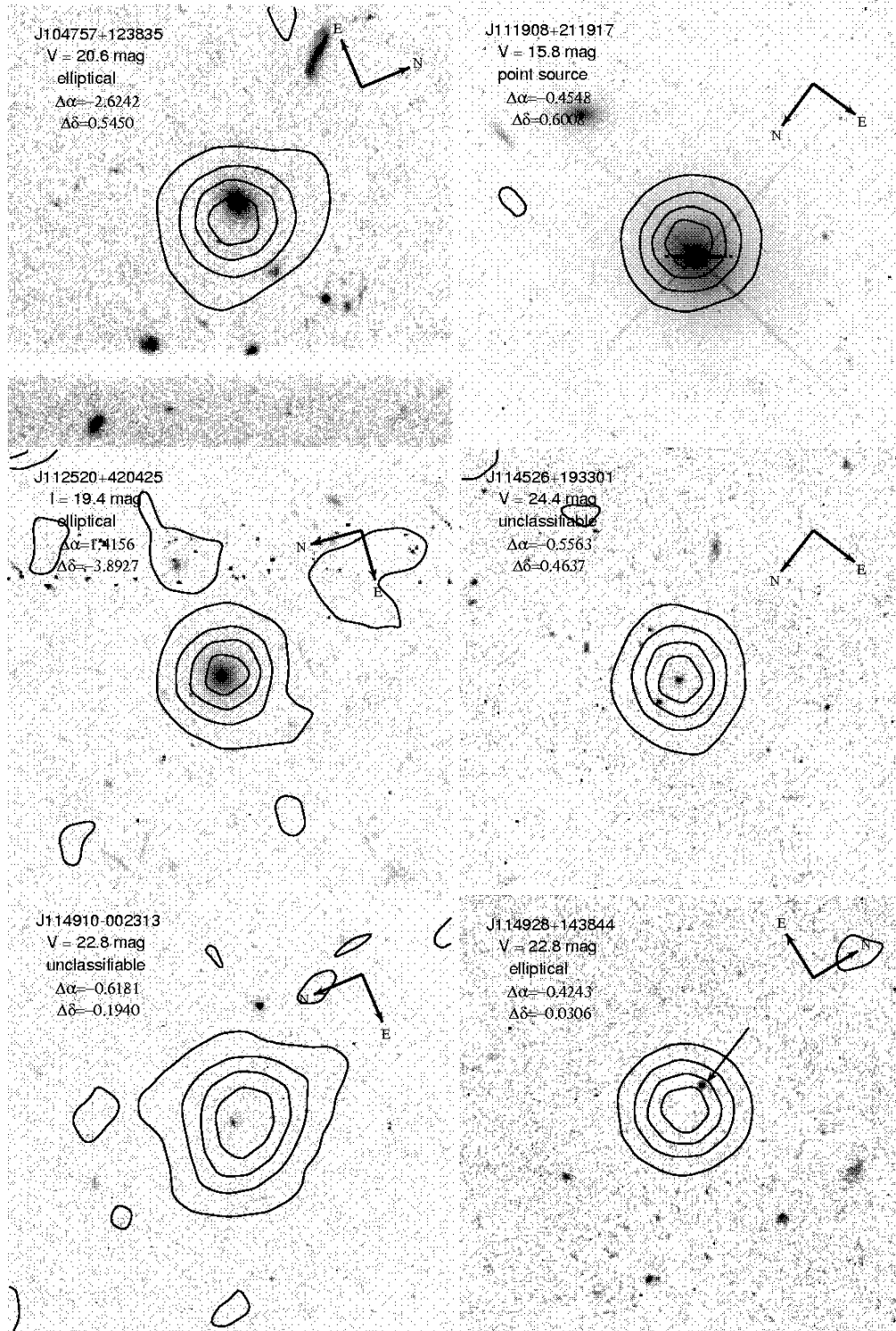
^cSérsic index (n) defined by the equation (6).

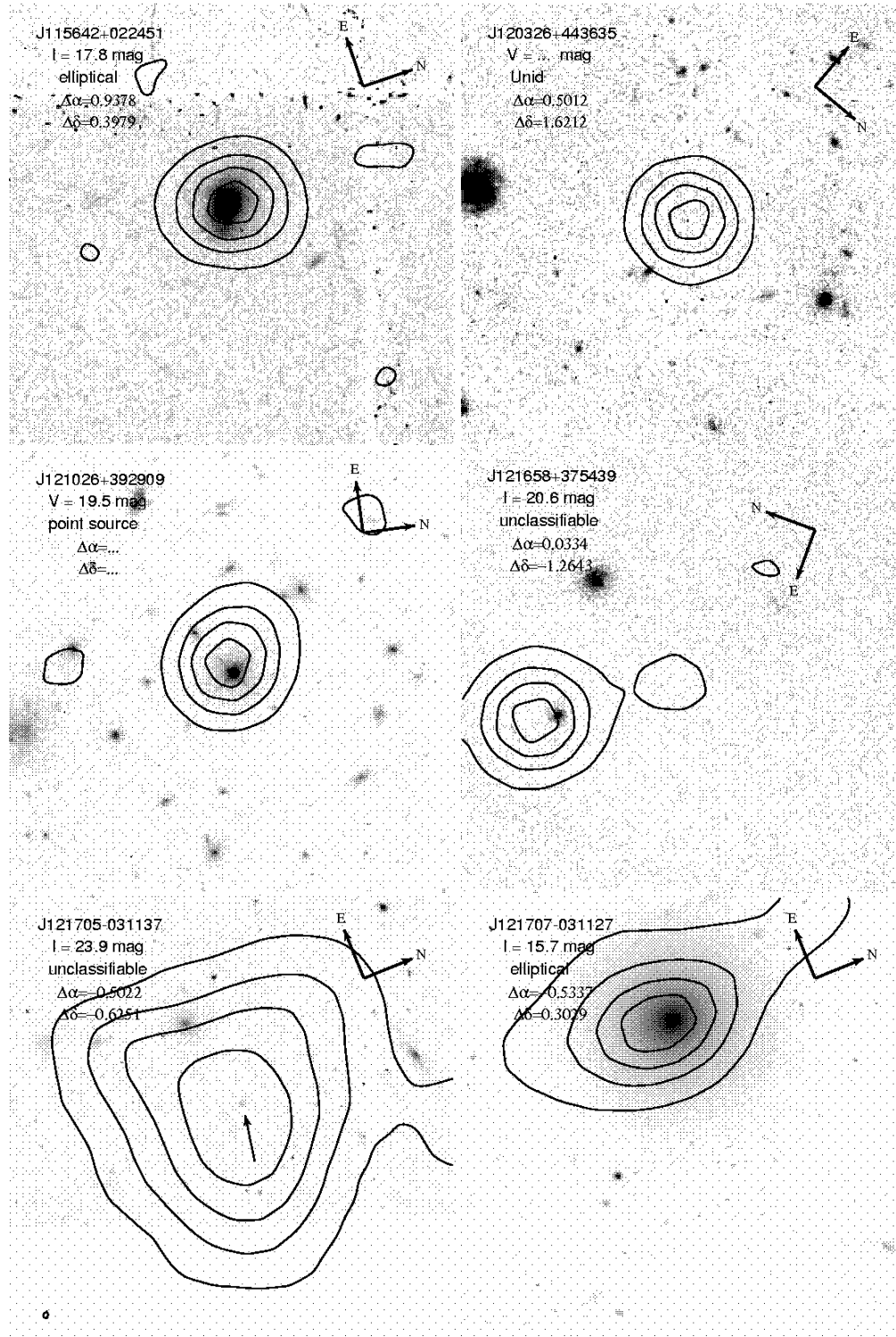
^dReduced χ_ν^2 between the observed profile and equation (6).

^eArtificial Neural Network type classification as measured by LMORPHO (Odewahn et al. 1996)

^fMorphology of optical counterpart. ‘x’ used to classify objects too small to assign a reliable morphology. ‘xC’ indicates the object is compact. ‘xE’ indicates the object is extended. ‘*’ indicates a unique note for that source.

^gThis is the header keyword for the field target from the WFPC2 images, which helped us assess the “randomness” of each WFPC2 field.



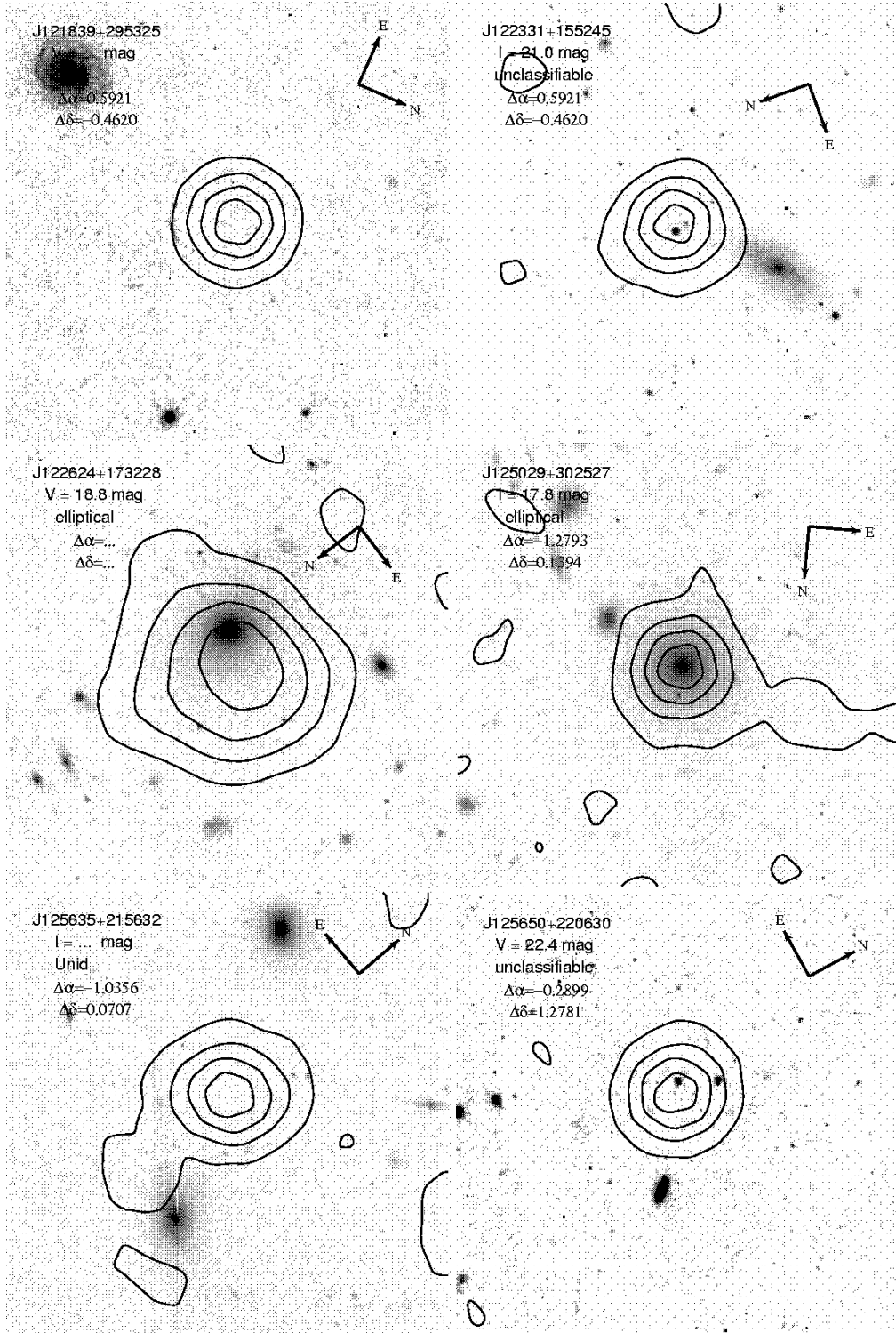


3.2. Optical Magnitude Distribution

We measure optical fluxes from the HST-WFPC2 images, using the software package LMORPHO (Odewahn et al. 1996), which we list in Table 4. In Figure 4, we show the distributions of the V - and I -band apparent magnitudes. While the statistics may be relatively low, these distributions clearly peak at $V \simeq 22$ mag and $I \simeq 26$ mag, which is in each plot several magnitudes brighter than the typical field depth. These peaks are similar to the what was observed in the LBDS (Windhorst et al. 1984b), and its Hercules subfield (Waddington et al. 2000), which are

only complete to $V \simeq 22.7$ mag and $I \simeq 21$ mag, respectively. Since our compendium of HST-WFPC2 fields are generally ~ 2 mag deeper than the optical imaging in the LBDS, these peaks in the magnitude distributions are more secure than reported in those earlier works, which were based on ground-based photographic or CCD imaging and poorer seeing. Furthermore, in the microjansky flux range, Hammer et al. (1995a) find similar peaks in the apparent magnitude distributions in the Canada-France Redshift Survey (CFRS).

Since for a given object only HST/WFPC2 V - or I -

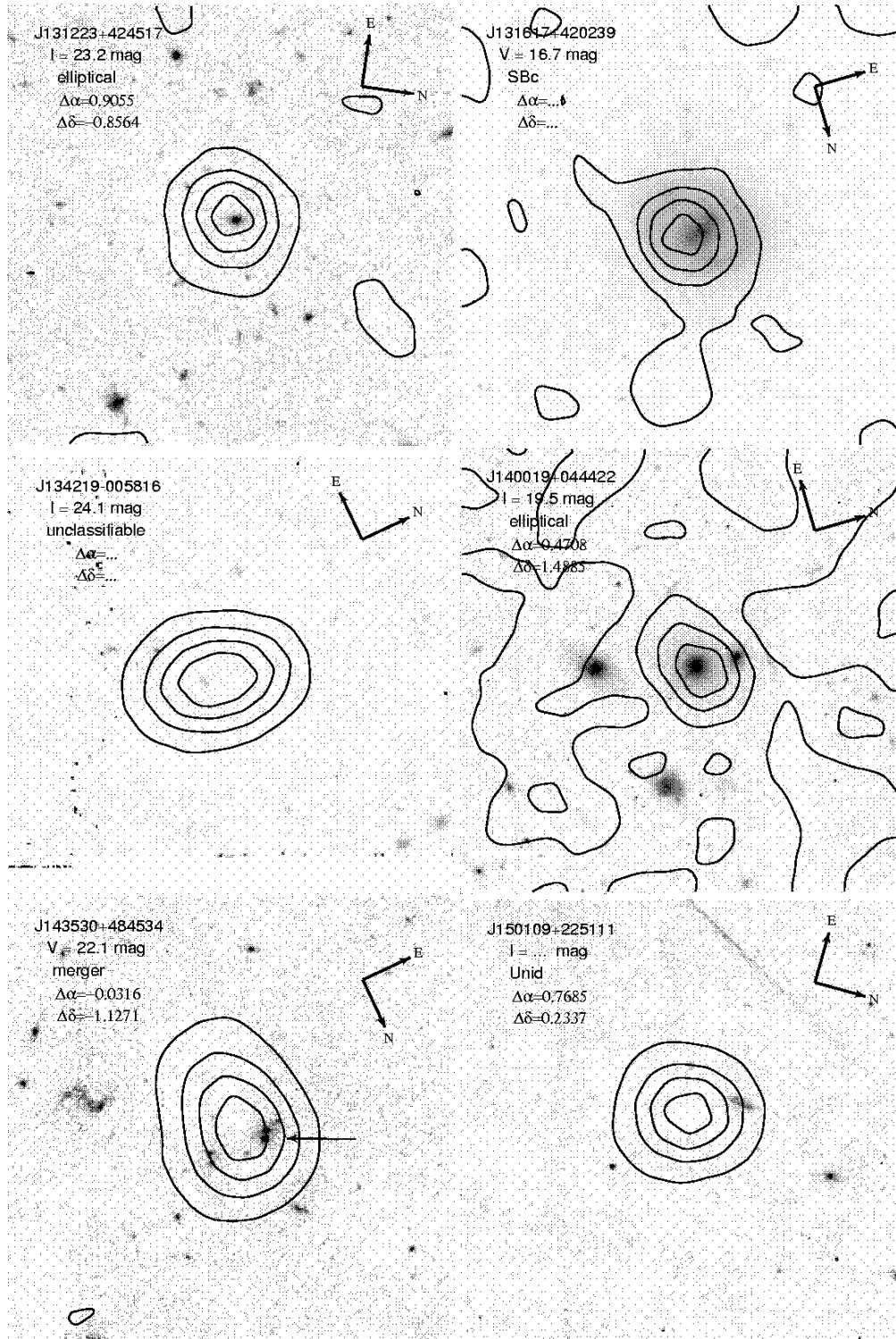


band imaging is available, we require an algorithm to convert the observed flux in one bandpass to what is expected in the other. Therefore, we retrieve the g' -, r' -, and i' -fluxes for 22/43 galaxies available from the Sloan Digital Sky Survey, Data Release 5 (SDSS-DR5; Adelman-McCarthy et al. 2007). The g' - and r' -band fluxes are converted to an effective V -band for a typical galaxy spectral energy distribution (SED) following Jester et al. (2005):

$$V_{\text{eff}} = g' - 0.59 \times (g' - r') - 0.01 \text{ (mag)}. \quad (7)$$

In Figure 5, we show the SDSS i' -band flux as a func-

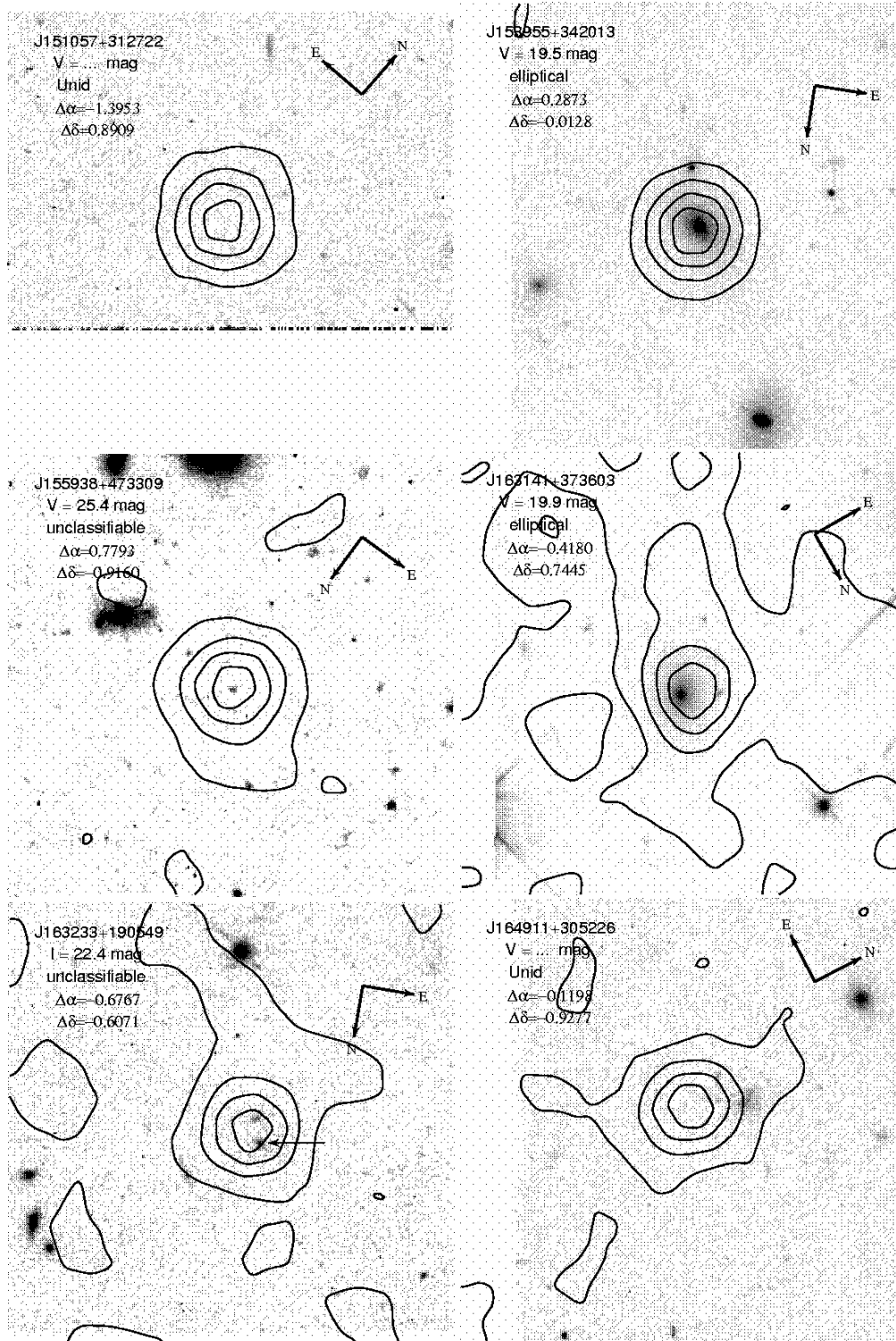
tion of the effective V -band flux, as synthesized from the SDSS g' - and r' -band observations and the best-fit, linear model to fit of $i' = (1.85 \pm 0.02) + (0.86 \pm 0.00) \times V_{\text{eff}}$. To verify these conversions from g' and r' to V_{eff} and from i' to I , we show $\Delta V \equiv (V - V_{\text{eff}})$ and $\Delta I \equiv (I - i')$ as a function the respective HST observations in Figure 6. For galaxies which only have V -band WFPC2 data, the difference between the HST-WFPC2 and the effective V is $\langle \Delta V \rangle = 0.03 \pm 0.18$ mag, while the corresponding difference in the I -band is $\langle \Delta I \rangle = 0.03 \pm 0.25$ mag. This indicates that the correlation in Figure 5 can be used to sys-



tematically convert the WFPC2 V -band fluxes to corresponding I -band fluxes with an uncertainty of $\lesssim 0.3$ mag. This uncertainty is not large enough to affect any of our conclusions in a significant way.

With these converted fluxes, we show the I -band magnitude distribution for the 43 identified optical galaxies in Figure 7. To determine the location of the peak, we fit a simple Gaussian to magnitude distribution. The peak at $I \simeq 20.7 \pm 0.5$ mag is significantly brighter (~ 3 mag) than the completeness limit of our typical WFPC2 field, which suggests that this peak is not due to incomplete-

ness. This peak may reflect the redshift distribution, and possibly strong cosmological evolution of the radio source population. Waddington et al. (2000) point out that if the radio galaxies had the same space density at all redshifts, then we expect the number of galaxies per magnitude interval would increase toward the observational limit, as is roughly the case for the optical field galaxy counts. With the exceptional resolution and increased depth of the HST-WFPC2 dataset, we extend the typical limit of $AB \sim 22$ mag to $AB \sim 24$ mag for the millijansky population over a significant field-of-view.



This magnitude distribution is quite different than what is expected from a general population of field galaxies (Tyson 1988). The radio-selected galaxy counts likely peak at $I \simeq 20.7 \pm 0.5$ mag since the majority of millijansky sources have L^* -type luminosities at $z \sim 0.8$ (Condon 1989).

3.3. Radio-to-Optical Spectral Index

Kron, Koo, & Windhorst (1985) show that the radio-to-optical spectral index (α_{ro}) can be used to distinguish between red and blue galaxies. Therefore, we perform

a similar analysis with morphological types determined from the high-resolution imaging. In Figure 8, we show the I -band flux as a function of the radio flux for the 43 optically identified galaxies. Objects are separated into three classes by their optical morphology (discussed in § 3.1) of early, late, and unclassifiable as filled red circles, green triangles, and blue squares, respectively. We show lines of constant radio-to-optical spectral index

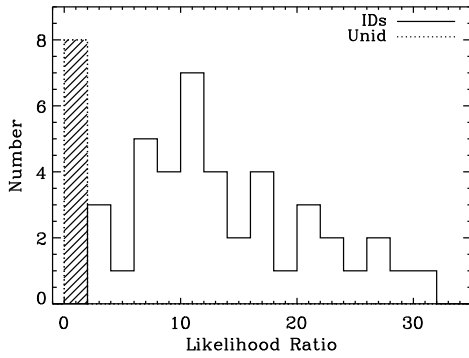
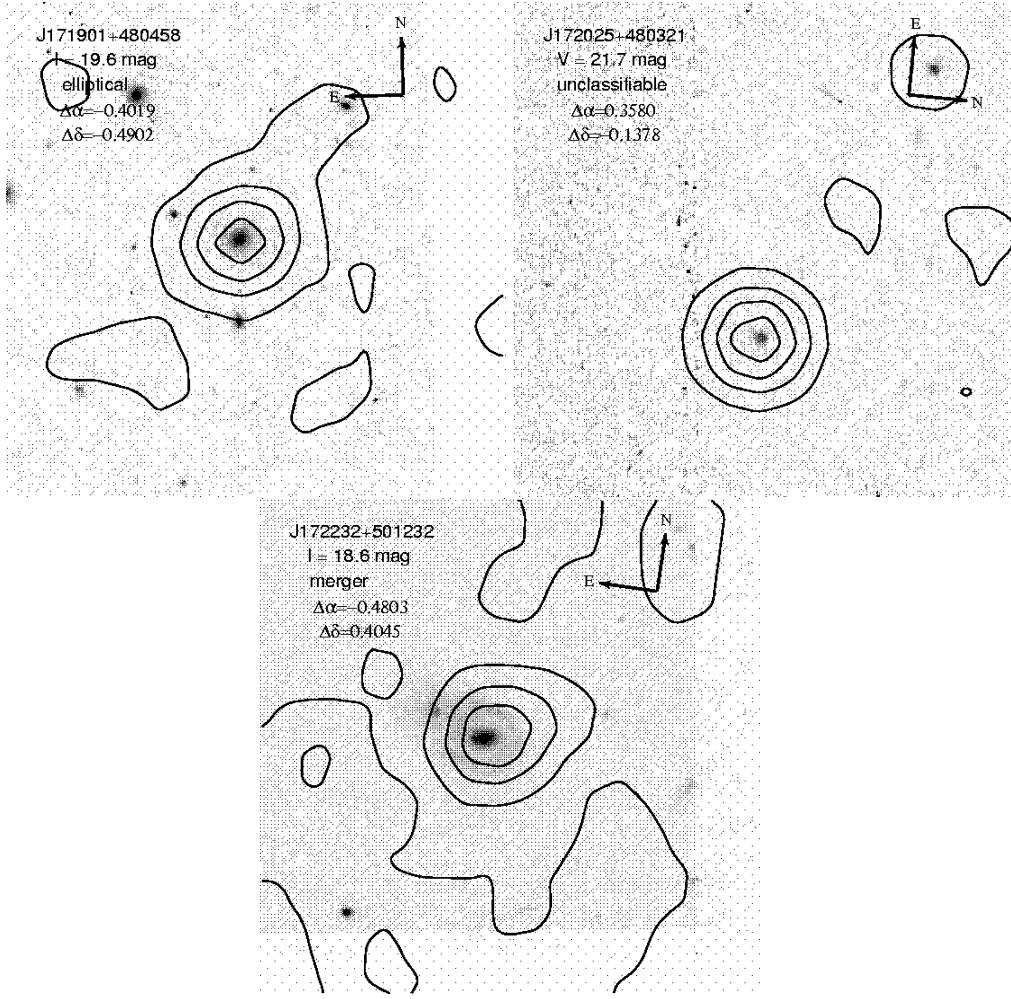


FIG. 3.— Distribution of likelihood ratios, LR as defined by equation (1). We compute the likelihood that a radio source has a given optical counterpart following de Ruiter et al. (1977), which is summarized in § 2.4. We show all radio sources which were positively identified with an optical counterpart as a solid distribution. The unidentified galaxies are represented as a hatched distribution. As argued in the text, every positively identified object has $LR \geq 2$, while the unidentified galaxies have $LR \ll 2$. Note that two objects with $LR > 40$ are not represented.

defined by:

$$\alpha_{ro} = \frac{\log(S_{1.4}/S_I)}{\log(20.4 \text{ cm}/8012 \text{ \AA})} \quad (8)$$

$$= 0.185 \times \log(S_{1.4}/S_I), \quad (9)$$

where $\log(S_I/1\text{Jy}) = -0.4 \times (I - 8.72) \text{ mag}$ (Oke & Gunn 1983). The solid lines denote logarithmic radio-to-optical

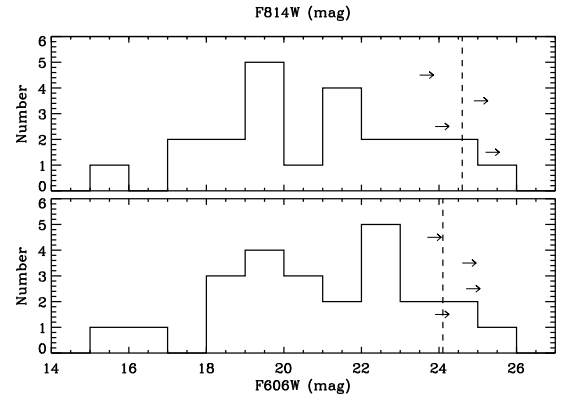


FIG. 4.— Optical WFPC2 magnitude distributions, separated by bandpass (top: V -band, bottom: I -band). The arrows represent the depth for fields where no optical counterpart could be identified. The vertical dashed line shows the flux-averaged, 50% completeness limit for each bandpass. These magnitude distributions peak $\gtrsim 2 \text{ mag}$ brighter than the average completeness limit for the average WFPC2 field. While the statistics may be relatively low, this suggests that the turn-over in the optical magnitude distributions from earlier studies was not due to their shallow imaging.

flux ratios from 1 to 10^5 . In general, the elliptical galaxies (filled red circles) have $I \lesssim 20 \text{ mag}$ and shallower spectral indices of $\alpha_{ro} \lesssim 0.4$. Conversely, the unclassifiable galaxies (filled blue squares) have $\alpha_{ro} \gtrsim 0.4$, which is primarily due to their brightnesses ($I \gtrsim 21 \text{ mag}$). Furthermore, since these galaxies span the entire range of radio fluxes, they are likely representative of the gen-

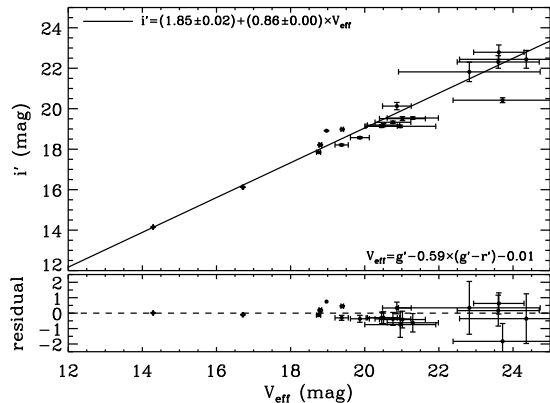


FIG. 5.— Colors of FIRST radio galaxies in our sample from SDSS-DR5. The *effective V*-band is constructed following Jester et al. (2005) as a combination of the SDSS g' - and r' -bandpasses, which we give in the lower-right corner of the upper panel. The solid line represents the best-fit linear model to the data, which is given in the upper-left corner of the upper panel. The lower panel shows the residuals, as the observations minus the model. The average color for these radio galaxies from the SDSS database is $\langle i' - V_{\text{eff}} \rangle \simeq 1.8$ mag.

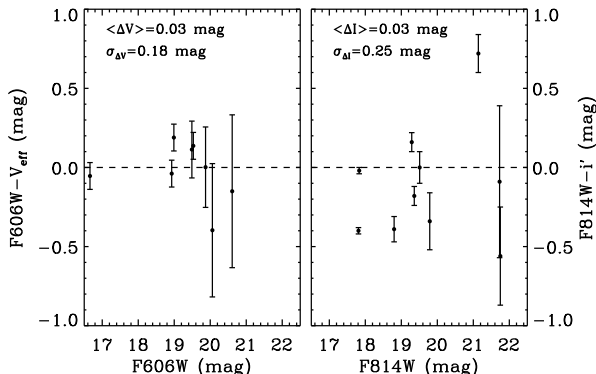


FIG. 6.— Comparison of the fluxes from SDSS-DR5 and HST-WFPC2 observations. These panels show the ratio between the HST and the SDSS fluxes as a function of the HST flux. The average difference and standard deviation are listed in the lower-right of each panel. In the left panel, we show the $(F606W - V_{\text{eff}})$ residual for the objects which were only observed in the V -band and had SDSS data. Since the average difference is only -0.08 ± 0.79 mag, the conversion from g' and r' to V_{eff} , and hence the correlation shown in Figure 5 is relatively robust. The right panel shows that the once the V -band measurements are converted to the i' -band, there is relatively little additional error introduced by assuming that $i' \approx I$ for these radio galaxies.

eral radio sample. Their lower optical fluxes could be caused by an increased dust obscuration associated with a surrounding starburst and/or enhanced/beamed radio emission. Deep infrared observations would be capable distinguishing these two scenarios, and likely detect the 8/43 optically unidentified radio galaxies.

In the GOODS-S field (Giavalisco et al. 2004), Afonso et al. (2006) publish the optical and radio brightnesses for their sample of 43 optically-identified microjansky radio galaxies with morphological classifications. In Figure 8, we show their microjansky radio galaxies as open symbols, where late-type and star-forming galaxies generally constitute a much larger fraction of radio galaxies than at the millijansky level. Moreover, these late-type galaxies generally have $\alpha_{r_o} \lesssim 0.2$, which is a region of $(\alpha_{r_o} - I)$ parameter space where few early-type galaxies are found in our millijansky sample. For galaxies sufficiently re-

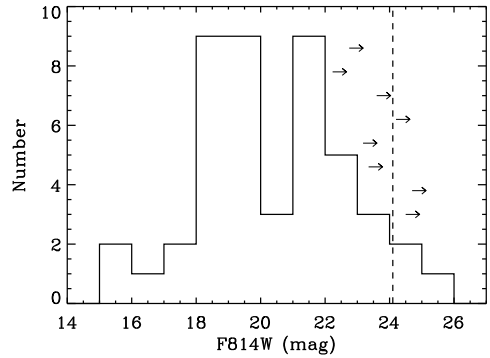


FIG. 7.— I -band magnitude distribution for all identified radio galaxies. The fluxes of sources where only V -band observations are available are converted assuming the SDSS-DR5 colors described in § 3.2, Figure 5, and Figure 6. The vertical dashed line shows the flux-averaged, 50% completeness depth of the fields, while the arrows represent the depths of the eight fields where no optical counterpart was identified to their respective field limits. This peak at $I \simeq 20.7 \pm 0.5$ mag is nearly 3 mag brighter than the depth of the typical WFPC2 field. The source counts of a random population of field galaxies should increase as a power-law to the completeness limit of the field, contrary to what is seen for the radio selected galaxies.

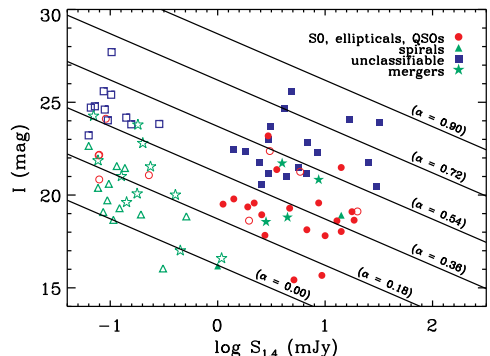


FIG. 8.— Integrated radio flux versus total I -band magnitude for the complete FIRST+WFPC2 sample. The V -band flux has been converted to an effective I -band as described in § 3.2. Objects are separated into early, late, merger, and unclassifiable types, while the filled and open symbols are from this work and Afonso et al. (2006), respectively. The lines are contours of constant radio-to-optical flux ratios as defined by equation (8). In the millijansky flux range, the majority of the galaxies have early-type morphologies and shallow spectral slopes of $\alpha_{r_o} \lesssim 0.4$. Additionally, there is only one late-type spiral and 4 mergers which span a large range of spectral indices ($0 \lesssim \alpha_{r_o} \lesssim 0.5$). However, lower radio fluxes ($S_{1.4} \ll 1$ mJy), there are very few early-type systems where late-type systems dominate the counts with the $\alpha_{r_o} \lesssim 0.4$. This dramatic change in optical morphologies at $S_{1.4} \simeq 1$ mJy may be related to a change in the source of the radio emission, such as primarily starburst galaxies ($S_{1.4} \lesssim 1$ mJy) versus primarily AGN ($S_{1.4} \gtrsim 1$ mJy). Additionally, the line of $\alpha_{r_o} \simeq 0.18$ marks a fiducial point, below which nearly all galaxies are late-type.

solved and given a reliable optical classification, spirals and mergers dominate the radio source counts at the microjansky level (25/43, 53%) while early-type galaxies are the dominant type at millijansky fluxes (19/25, 76%).

3.4. Optically Unidentified Radio Sources (Unids)

For the sample of 51 FIRST sources, eight were found to have no optical counterpart identifiable to $AB \sim 23.6 - 25.0$ mag (see Table 4 for 50% depths of each field from the Snigula method described in § 2.4). Like

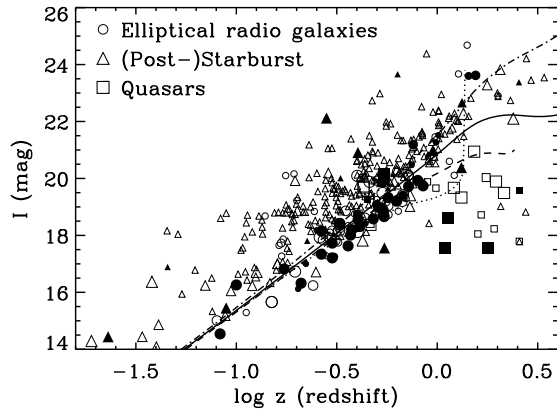


FIG. 9.— The Hubble diagram for faint radio galaxies. Data is compiled from numerous sources (Windhorst et al. 1984b; Kron, Koo, & Windhorst 1985; Windhorst et al. 1985; Fomalont et al. 1997; Richards et al. 1998; Waddington et al. 2001; Roche et al. 2002; Chapman et al. 2003). The circles, triangles, and squares represent ellipticals, starbursts, and quasars, respectively. The open symbols represent point-like or small radio sources, while filled symbols show (classical) double or extended radio sources; the size of the plotted point is logarithmically proportional to the radio flux from $10 - 10^3$ microjansky (Windhorst 2003). The lines are from stellar population synthesis models of (Bruzual & Charlot 2003). The dot-dashed line is a constant star-formation model and solid, dashed, and dotted lines are an exponential star-forming history with ages of 13, 11, and 9 Gyr, respectively. The e -folding timescale in the exponential models is 1.3 Gyr. All models assume a stellar mass of $10^{11} M_{\odot}$, a Salpeter IMF (Salpeter 1955), and solar metallicity. The obvious trend in this diagram suggests that early-type radio galaxies are roughly standard candles, and that the unidentified millijansky objects with $I \gtrsim 22$ mag are likely at $z \gtrsim 1$. NOTE: The I -band magnitudes in this figure are in the Vega system, when necessary we assume $(I_{AB} - I_{Vega}) \simeq 0.48$ mag.

the unclassifiable galaxies, the unidentified objects have radio fluxes which span a comparable range to the entire radio sample (see Table 3) and thus may be representative of the general population. However, unlike the unclassifiables, their lack of any optical flux may indicate that they are considerably higher redshift. In Figure 9, we show the Hubble diagram (I -band flux as a function of redshift) for all faint radio galaxies, where the size of the plotted symbol is logarithmically proportional to the radio flux (see Windhorst 2003, for more details). From Figure 9, millijansky radio sources with an optical counterpart with a brightness of $I \gtrsim 22$ mag are likely at $z \gtrsim 1$ (eg. Schmidt, Connolly, & Hopkins 2006), indicating that these galaxies may be standard candles. However, the significant spread in redshift for galaxies with $I \gtrsim 22$ mag suggests that an additional effect may be present, which could be an increased optical extinction, different stellar populations at high redshift, or significant luminosity evolution. Without a robust optical detection of these galaxies, we can only speculate about their counterparts. Based on the Hubble diagram, these optically unidentified galaxies could be similar to the distant red galaxies (DRGs; Förster Schreiber et al. 2004; van Dokkum et al. 2006; Georgakakis et al. 2006; Schmidt, Connolly, & Hopkins 2006) at $z \simeq 2$. The DRGs are generally old, dusty, and massive galaxies with very red infrared colors ($I - J \gtrsim 2$ mag, $J - H \sim 2$ mag, and $H - K \sim 1$ mag). Therefore, near-infrared observations are ideal for identifying the optical/infrared counterpart.

4. COMMENTS ON INDIVIDUAL RADIO SOURCES

We give brief comments on each of the 51 radio sources in the sample and their most likely optical identification (where applicable). We note the overlap with previous works where available found from the NASA/IPAC Extragalactic Database⁴.

1. **J002219.1–013030**: Unclassifiable. The optical counterpart is entirely visible despite being near the edge of the WFPC2 field. The object is also within $18''$ of a NVSS radio source (Condon et al. 1998).
2. **J004322.3–001343**: Point-source. This object was identified as a quasar in the SDSS (Richards et al. 2004).
3. **J012616.6–012126**: Late-type, barred spiral (type SBb-SBc). This object is a bright ($V \simeq 19.8$ mag) and well-resolved mid-late type spiral galaxy.
4. **J030237.6+000818**: Unidentified with $I \geq 24.5$ mag. There are four CFRS objects within $30''$ (Hammer et al. 1995b).
5. **J030249.5+000615**: Elliptical. There is no noticeable optical elongation to indicate any alignment of the radio source within the galaxy. Hammer et al. (1995b) classified this source as an E0.
6. **J082820.6+344321**: Unclassifiable. The optical candidate is very faint ($I \simeq 25.6$ mag).
7. **J082828.4+344131**: Unidentified with $I \geq 24.7$ mag.
8. **J084715.5+443752**: Unclassifiable. The radio source is clearly extended and was found by Windhorst et al. (1985).
9. **J084849.5+445550**: Elliptical. There is no evidence for any optical elongation with the resolved radio source. The object is located in a group or poor cluster, and the shape of radio contours were used to determine the identification. This object was also identified by Oort (1987).
10. **J091205.2+350506**: Unclassifiable. The optical source is extended and very faint ($V \simeq 23.8$ mag), and is near a bright star.
11. **J091251.0+525928**: Unclassifiable. The optical counterpart is small, and possibly extended. The radio counters are clearly elongated.
12. **J094926.6+295941**: Elliptical. The optical and radio emission is not aligned.
13. **J094930.7+295938**: S0. The radio source is clearly double-lobed and the optical identification is slightly off the radio axis, the radio contours appear to be somewhat “bent” toward the identified object.

⁴ NED is operated by the Jet Propulsion Laboratory, California Institute of Technology, under contract with the National Aeronautics and Space Administration.

14. **J100354.5+285911**: Merger. The radio source is likely double-lobed with the merging system located at the center of the radio axis.
15. **J102437.2+470312**: Unclassifiable. The optical object is marginally extended.
16. **J102744.6+282921**: Unclassifiable. This object is very faint ($I \simeq 22.4$ mag) and on the outskirts of a bright spiral galaxy, which is $\sim 7''$ to the west. Therefore, the spiral galaxy center is likely *not* the optical identification. The radio source may be caused by a supernova remnant (eg. Windhorst et al. 1984b; Kron, Koo, & Windhorst 1985) or a background galaxy, which may be somewhat extinguished by the foreground spiral galaxy.
17. **J103452.3+394704**: Unclassifiable. The optical source is extended, likely a galaxy in a group.
18. **J104630.8-001213**: Merger. The merger pair is an elliptical and early-type disk galaxy, however neither show obvious signs of interaction. The optical candidate was in the sample of Glazebrook et al. (1995).
19. **J104757.0+123835**: Elliptical. The radio source is fairly round and was identified by Condon et al. (1998).
20. **J111908.6+211917**: Point source. This object was identified as a QSO by Barkhouse & Hall (2001).
21. **J112520.7+420425**: Elliptical/S0. The radio source is round and was identified by Condon et al. (1998).
22. **J114526.3+193301**: Unclassifiable.
23. **J114910.5-002313**: Unclassifiable.
24. **J114928.3+143844**: Elliptical. This galaxy was identified by Condon et al. (1998).
25. **J115642.8+022451**: Elliptical. The optical emission is roughly perpendicular to the radio contours. This object was identified by Condon et al. (1998).
26. **J120326.4+443635**: Unidentified with $V \geq 25.0$ mag.
27. **J121026.6+392909**: Point source. It is located in group and was classified as a QSO (Hewitt & Burbidge 1993).
28. **J121658.4+375439**: Unclassifiable. The optical source is marginally extended. The radio source may be double-lobed, but of very unequal lobe flux.
29. **J121705.5-031137**: Unclassifiable. The radio source is resolved.
30. **J121707.7-031127**: Elliptical. The optical emission is round, while the radio counters are elongated. This object was classified as an AGN in the SDSS (Richards et al. 2004).
31. **J121839.7+295325**: Unidentified with $V \gtrsim 24.8$ mag. The morphology of the nearby optical source suggests that it could be gravitationally lensed by the unidentified radio galaxy (Ryan et al. 2008b).
32. **J122331.0+155245**: Unclassifiable. This radio source was identified by Condon et al. (1998).
33. **J122624.4+173228**: Elliptical. This galaxy may have a companion to the east-north-east, and is in a small group. This radio galaxy was identified by Condon et al. (1998).
34. **J125029.2+302527**: Elliptical. This galaxy is like in a cluster or group. The radio source has round inner contours, but appears to be resolved on larger scales.
35. **J125635.3+215632**: Unidentified with $I \geq 24.2$ mag. There are three relatively bright objects within $\sim 4''$ of the radio source. The radio source was identified by Condon et al. (1998).
36. **J125650.0+220630**: Unclassifiable. The radio source was identified by Condon et al. (1998).
37. **J131223.6+424517**: Elliptical.
38. **J131617.8+420239**: Late-type barred spiral (SBc). This object is $\gtrsim 10''$ in diameter and is also an infrared source, identified in the Two Micron All Sky Survey (2MASS; Skrutskie et al. 2006).
39. **J134219.9-005816**: Unclassifiable.
40. **J140019.9+044421**: Elliptical. The object is located in the center of a small group. The radio contours are slightly elongated, while the optical emission is fairly round.
41. **J143530.0+484534**: Merger. The optical candidate is on innermost radio contour.
42. **J150109.7+225111**: Unidentified with $I \geq 23.6$ mag. There is a disk galaxy $\simeq 3''$ from the radio position that could be the optical counterpart. Since the astrometric correction for this field was small, the nearby disk galaxy is likely not related, owing to the large separation and the relatively low background object density.
43. **J151057.4+312722**: Unidentified with $V \geq 23.7$ mag.
44. **J153955.0+342013**: Elliptical. The optical emission is fairly elongated, while the radio contours are round. This system may have several companion systems to the south and west.
45. **J155938.7+473309**: Unclassifiable. This object may be located in a dense group of faint, small objects. This radio source was identified by Condon et al. (1998).
46. **J163141.4+373603**: Elliptical. The optical and radio emission appear to be aligned. The radio emission is part of a larger, low SB complex.

47. **J163233.8+190550**: Unclassifiable. The optical counterpart is the northern of the two small objects. This radio source was identified by Condon et al. (1998).
48. **J164911.4+305226**: Unidentified with $V \geq 24.3$ mag. There is a late type galaxy approximately $4''$ from the radio position, but given that the astrometric corrections are less than $2''$, and the $LR \sim 0.0$, this is considered an unidentified source.
49. **J171901.1+480458**: Elliptical. This radio source found in Condon et al. (1998).
50. **J172025.4+480331**: Unclassifiable. This object may be marginally extended.
51. **J172232.9+501232**: Merger. The primary galaxy is clearly a late-type, possibly barred spiral which shows clear signs of interaction. The secondary galaxy is considerably smaller and may also be a late-type disk system.

5. SUMMARY AND DISCUSSION

We have determined the optical morphology and structure from HST-WFPC2 imaging of a randomly-selected sample of 51 millijansky radio sources from the FIRST survey. Earlier studies of millijansky radio galaxies have often distinguished early- versus late-types based on observed optical colors or spectra. However, we have extended such works by providing optical classifications based on HST imaging, and confirm that elliptical galaxies constitute the majority of the millijansky source population.

We find that the optical flux distribution of these galaxies peaks at $I \simeq 20.7 \pm 0.5$ mag, which is consistent

with evolutionary model of Condon (1989): faint radio galaxies generally have L^* -type optical luminosities with a median redshift of $z \simeq 0.8$ and an effective redshift decline for $z \gtrsim 1.5$. At low redshift ($z \lesssim 1$), most radio sources brighter than $S_{1.4} \gtrsim 1$ mJy are generally found in massive ellipticals, and there is a clear deficit of these massive galaxies at $z \gtrsim 3$ (eg. Driver et al. 1998). De Lucia et al. (2006) argue that $\sim 50\%$ of the stars which will likely end up in elliptical galaxies in the local Universe are formed at $z \simeq 3$, and are not finally assembled into the galaxy until $z \simeq 0.8$. This down-sizing picture requires an increased major merger rate from $z \sim 0$ to $z \sim 3$, which has been observed in the Hubble Ultra Deep Field (eg. Ryan et al. 2008a). Finally, this effective redshift cut-off may arise, since ~ 1 Gyr may be on average required to trigger an active nucleus after the major merger based on hydrodynamical models (Springel et al. 2005). This must be further studied in the critical redshift range of $1 \lesssim z \lesssim 3$, which may prove useful in tracing the high-redshift evolution of the supermassive black hole–bulge mass relation (eg. Ferrarese & Ford 2005). At these redshifts, the optical counterparts will be extremely faint ($AB \gtrsim 25$ mag), and may have a high dust content or their luminosity function may evolve strongly or episodically with redshift. Consequently, dedicated observations with the Wide Field Camera 3 (WFC3) or the *James Webb Space Telescope* will be needed for the continued study of the population of millijansky radio sources.

The authors would like to thank the anonymous referee and Rolf Jansen for their constructive input and Tom Keck for his efforts. This work was supported in part by the NASA Space Grant, NSF grant AST-9802963, and NASA grants AR-8357.01A and AR-8768.01A from STScI under NASA contract NAS5-26555.

REFERENCES

- Afonso, J., Mobasher, B., Koekemoer, A., Norris, R. P., & Cram, L. 2006, *AJ*, 131, 1216
- Adelman-McCarthy, J. K. et al. 2007, *ApJS*, 172, 634
- Bahcall, J. A., Kirhakos, S., Saxe, D. H., & Schneider, D. P. 1997, *ApJ*, 479, 642
- Barkhouse, W. A., & Hall, P. B. 2001, *AJ*, 121, 2843
- Becker, R. H., White, R. L., & Helfand, D. J. 1995, *ApJ*, 450, 559
- Benn, C. R., Rowan-Robinson, M., McMahon, R. G., Broadhurst, T. J., & Lawrence, A. 1993, *MNRAS*, 263, 98
- Best, P. N., Kaufmann, G., Heckman, T. M., & Ivezić, Z. 2005, *MNRAS*, 362, 9
- Biretta, J. A., et al. 2000, *Wide Field Camera 2 Instrument Handbook, Version 5.0* (Baltimore: STScI)
- Bruzual, G., & Charlot, S. 2003, *MNRAS*, 344, 1000
- Casertano, S., et al. 2000, *AJ*, 120, 2747
- Chapman, S. C., et al. 2003, *ApJ*, 585, 57
- Cohen, S. H., Windhorst, R. A., Odewahn, S. C., Chiarenza, C. A. T., & Driver, S. P. 2003, *AJ*, 125, 1762
- Condon, J. J. 1989, *ApJ*, 338, 13
- Condon, J. J., Cotton, W. D., Greisen, E. W., Yin, Q. F., Perley, R. A., Taylor, G. B., & Broderick, J. J. 1998, *AJ*, 115, 1693
- De Lucia, G., Springel, V., White, S. D. M., Croton, D., & Kauffmann, G. 2006, *MNRAS*, 366, 499
- Dey, A., Spinrad, H., & Dickenson, M. 1995, *ApJ*, 440, 515
- Driver, S. P., Fernandez-Soto, A., Couch, W. J., Odewahn, S. C., Windhorst, S. C., Phillips, S., Lanzetta, K. & Yahil, A. 1998, *ApJ*, 496, L93
- Driver, S. P., et al. 2006, *MNRAS*, 368, 414
- Ferrarese, L. & Ford, H. 2005, *SSR*, 116, 523
- Fomalont, E. B., Kellermann, K. I., Richards, E. A., Windhorst, R. A., & Partridge, R. B. 1997, *ApJ*, 475, L5
- Förster Schreiber, N. M. et al. 2004, *ApJ*, 616, 40
- Gardner, J. P., & Satyapal, S. 2000, *AJ*, 119, 2589
- Georgakakis, A., Hopkins, A. M., Afonso, J., Sullivan, M., Mobasher, B., & Cram, L. E. 2006, *MNRAS*, 367, 331
- Gialalisco, M., et al. 2004, *ApJ*, 600, L93
- Glazebrook, K., Ellis, R., Colless, M., Broadhurst, T., Allington-Smith, J., & Tanvir, N. 1995, *MNRAS*, 273, 157
- Graham, A. W. & Driver, S. P. 2005, *PASA*, 2005, 22, 118
- Hales, S. E. G., Baldwin, J. E., & Warner, P. J. 1988, *MNRAS* 234, 919
- Hammer, F., Crampton, D., Lilly, S. J., Le Fevre, O., & Kenet, T. 1995, *MNRAS*, 276, 1085
- Hammer, F., Crampton, D., Le Fevre, O., & Lilly, S. J. 1995, *ApJ*, 455, 88
- Hewitt, A. & Burbidge G. 1993, *ApJS*, 87, 451
- Holtzman, J. A., Burrows, C. J., Casertano, S., Hester, J. J., Traugher, J. T., Watson, A. M., & Worthey, G. 1995, *PASP*, 107, 1065
- Hopkins, A. M., Afonso, J., Chan, B., Cram, L. E., Georgakakis, A., & Mobasher, B. 2003b, *RMxAC*, 17, 252
- Hopkins, A. M. & Beacom, J. F. 2006, *ApJ*, 651, 142
- Ivezić, Z. et al. 2002, *ApJ*, 124, 2364
- Jester, S., et al. 2005, *AJ*, 130, 873
- Kron, R. G., Koo, D. C., & Windhorst, R. A. 1985, *A&A*, 146, 38
- Lowenthal, J. D. 1997, *RMxAC*, 6, 105
- Mackay, C. D., 1971, *MNRAS*, 154, 209
- Machalski, J., & Godlowski, W. 2000, *A&A*, 360, 463
- Mainieri, V., et al. 2008, *ApJS*, accepted
- McCarthy, P. J., Miley, G. K., de Koff, S., Baum, S. A., Sparks, W. B., Golombek, D., Biretta, J., & Macchetto, F. 1997, *ApJS*, 112, 415
- Metcalfe, N., Shanks, T., Campos, A., Fong, R., & Gardner, J. P. 1996, *Nature*, 383, 236

- Monet, D., et al. 1996, USNO-SA2.0, (U.S. Naval Observatory, Washington DC)
- Odewahn, S. C., Windhorst, R. A., Driver, S. P., & Keel, W. C. 1996, *ApJ*, 472, L13
- Oke, J. B. & Gunn, J. E. 1983, *ApJ*, 266, 713
- Oort, M. J. A. 1987, *A&ASS*, 71, 221
- Overzier, R. A., Röttgering, H. J. A., Rengelink, R. B., & Wilman, R. J. 2003, *A&A*, 405, 53
- Pascarelle, S. M., Windhorst, R. A., Driver, S. P., Ostrander, E. J., & Keel, W. C. 1996, *ApJ*, 456, L21
- Richards, E. A., Kellerman, K. I., Fomalont, E. B., Windhorst, R. A., & Partridge, R. B. 1998, *AJ*, 116, 1039
- Richards, G. T., et al. 2004, *ApJS*, 155, 257
- Roche, N. D., Lowenthal, J. D., & Koo, D. C. 2002, *MNRAS*, 330, 307
- de Ruiter, H. R., Willis, A. G., Arp, H. C. 1977, *A&ASS*, 28, 211
- Ryan, R. E., Jr., Cohen, S. H., Windhorst, S. H., & Silk, J. 2008a, *ApJ*, 678, 751
- Ryan, R. E., Jr., Cohen, S. H., Windhorst, R. A., Keeton, C. R., & Veach, T. V. 2008b, *ApJ*, accepted, astro-ph/0806.3781
- Salpeter, E. E. 1955, *ApJ*, 121, 161
- Schmidt, S. J., Connolly, A. J., & Hopkins, A. M. 2006, *ApJ*, 649, 63
- Skrutskie, M. F., et al. 2006, *ApJ*, 131, 1163
- Snigula, J., Drory, N., Bender, R., Botzler, C. S., Feulner, G., & Hopp, U. 2002, *MNRAS*, 336, 1329
- Springel, V., Di Matteo, T., & Hernquist, L. 2005, *MNRAS*, 361, 776
- Tyson, J. A. 1988, *AJ*, 96, 1
- van Dokkum, P. G., et al. 2006, *ApJ*, 638, L59
- Waddington, I., Windhorst, R. A., Cohen, S. H., Partridge, R. B., Spinrad, H., & Stern, D. 1999, *ApJ*, 526, L77
- Waddington, I., Windhorst, R. A., Dunlop, J. S., Koo, D. C., & Peacock, J. A. 2000, *MNRAS*, 317, 801
- Waddington, I., Dunlop, J. S., Peacock, J. A., & Windhorst, R. A. 2001, *MNRAS*, 328, 882
- Waddington, I., et al. 2002, *MNRAS*, 336, 1342
- Windhorst, R. A., van Heerde, G. M., & Katgert, P. 1984a, *A&ASS*, 58, 1
- Windhorst, R. A., Kron, R. G., & Koo, D. C. 1984b, *A&ASS*, 58, 39
- Windhorst, R. A., Miley, G. K., Owen, F. N., Kron, R. G., & Koo, D. C. 1985, *ApJ*, 289, 494
- Windhorst, R. A., Mathis, D., & Neuschaefer, L. 1990, *ASPC*, 10, 389
- Windhorst, R. A. 2003, *NewAR*, 47, 357
- Yasuda, N., et al. 2001, *AJ*, 122, 1104